



Neoproterozoic glacial origin of the Great Unconformity

C. Brenhin Keller^{a,b,1}, Jon M. Husson^c, Ross N. Mitchell^d, William F. Bottke^e, Thomas M. Gernon^f, Patrick Boehnke^{g,h}, Elizabeth A. Bellⁱ, Nicholas L. Swanson-Hysell^b, and Shanan E. Peters^j

^aBerkeley Geochronology Center, Berkeley, CA 94709; ^bDepartment of Earth and Planetary Science, University of California, Berkeley, CA 94720; ^cSchool of Earth and Ocean Sciences, University of Victoria, Victoria, BC V8W 2Y2, Canada; ^dDepartment of Applied Geology, Curtin University, Perth, WA 6845, Australia; ^eSouthwest Research Institute, Boulder, CO 80302; ^fOcean and Earth Science, University of Southampton, Southampton SO17 1BJ, United Kingdom; ^gDepartment of the Geophysical Sciences, The University of Chicago, Chicago, IL 60637; ^hChicago Center for Cosmochemistry, Chicago, IL 60637; ⁱDepartment of Earth, Planetary, and Space Sciences, University of California, Los Angeles, Los Angeles, CA 90095; and ^jDepartment of Geoscience, University of Wisconsin–Madison, Madison, WI 53706

Edited by Paul F. Hoffman, University of Victoria, Victoria, BC, Canada, and approved November 29, 2018 (received for review March 21, 2018)

The Great Unconformity, a profound gap in Earth's stratigraphic record often evident below the base of the Cambrian system, has remained among the most enigmatic field observations in Earth science for over a century. While long associated directly or indirectly with the occurrence of the earliest complex animal fossils, a conclusive explanation for the formation and global extent of the Great Unconformity has remained elusive. Here we show that the Great Unconformity is associated with a set of large global oxygen and hafnium isotope excursions in magmatic zircon that suggest a late Neoproterozoic crustal erosion and sediment subduction event of unprecedented scale. These excursions, the Great Unconformity, preservational irregularities in the terrestrial bolide impact record, and the first-order pattern of Phanerozoic sedimentation can together be explained by spatially heterogeneous Neoproterozoic glacial erosion totaling a global average of 3–5 vertical kilometers, along with the subsequent thermal and isostatic consequences of this erosion for global continental freeboard.

Great Unconformity | snowball Earth | glacial erosion | zircon | Cambrian explosion

Earth's sedimentary cover necessarily rests at depth upon igneous or metamorphic crystalline basement. This contact need not be abrupt, since accumulating sediments gradually recrystallize and metamorphose under increasing heat and pressure. Where observed, however, this transition often takes the form of a spatially abrupt and temporally correlated exposure surface known as the Great Unconformity, a lacuna of both time and mass (1–5). While often deeply buried, the Great Unconformity is exposed in areas of relief such as the Grand Canyon of the southwestern United States, where it was first recognized by Powell et al. (1), most dramatically at the sharp nonconformity between the Paleoproterozoic Vishnu Schist and Cambrian Tapeats Sandstone (6). The ubiquity of this pattern—undeformed clastic sediments deposited directly and unconformably atop Precambrian basement—was subsequently recognized by Walcott (2). Observing a dearth of conformable sections spanning the lower boundary of the Cambrian, Walcott proposed a “Lipalian” interval of continental exposure and erosion, which would have restricted any fossil precursors of the Cambrian fauna to the deep ocean basins. Subsequent investigation has revealed a more complete Proterozoic, including fossiliferous strata and conformable boundary sections; yet the observation of a profound and extensive (if discontinuous) pre-Cambrian unconformity remains (refs. 4 and 5 and Dataset S1). Here we attempt to unite disparate evidence including the zircon Hf and O isotope records, the terrestrial bolide impact record, and the record of continental sediment coverage in the context of this widespread unconformity.

A Discontinuous Global Unconformity

The extent and magnitude of secular variation in preserved sediment abundance across the Proterozoic–Phanerozoic boundary were first quantified by Ronov et al. (ref. 4 and Dataset S2), estimating preserved sediment volume flux over the past 1.6 Gy from mapped sedimentary basin areas and stratigraphic thicknesses. The resulting temporal pattern has been subsequently refined in Laurentia by the Macrostrat database (7–9) which (within North America) provides higher-resolution temporal and spatial constraints. Together these records corroborate the presence of a large global shift in preserved continental sediment abundance near the base of the Cambrian (Fig. 1A and SI Appendix, Figs. S1–S3).

The observed increase from roughly 0.2 km³/y of preserved sedimentary rock in the Proterozoic to ~1 km³/y in the Phanerozoic (Fig. 1A) might be attributed in principle to either constructive (faster sediment accumulation in the Phanerozoic) or destructive (erosion of Proterozoic strata) processes. However, the abrupt nature of the observed transition presents difficulties

Significance

It has long been observed that the sequence of sedimentary rocks deposited in the past half-billion years often sharply overlies older igneous or metamorphic basement at an erosional surface known as the Great Unconformity. We provide evidence that this unconformity may record rapid erosion during Neoproterozoic “snowball Earth” glaciations. We show that the extent of Phanerozoic sedimentation in shallow continental seas can be accurately reproduced by modeling the accommodation space produced by the proposed glacial erosion, underlining the importance of glaciation as a means for lowering erosional base level. These results provide constraints on the sedimentary and geochemical environment in which the first multicellular animals evolved and diversified in the “Cambrian explosion” following the unconformity.

Author contributions: C.B.K., J.M.H., and S.E.P. designed research; C.B.K. and J.M.H. performed research; C.B.K., J.M.H., R.N.M., W.F.B., T.M.G., P.B., E.A.B., N.L.S.-H., and S.E.P. analyzed data; R.N.M., W.F.B., and T.M.G. contributed the impact record; P.B. and E.A.B. contributed zircon Hf and O isotope data; N.L.S.-H. provided geological context; and C.B.K. wrote the paper.

Conflict of interest statement: The editor, P.F.H., is an adjunct professor in the same department as J.M.H.

This article is a PNAS Direct Submission.

This open access article is distributed under Creative Commons Attribution License 4.0 (CC BY).

Data deposition: Code for this article has been deposited in Github, <https://github.com/brenhinkeller/GreatUnconformity>.

¹To whom correspondence should be addressed. Email: cbkeller@dartmouth.edu.

This article contains supporting information online at www.pnas.org/lookup/suppl/doi:10.1073/pnas.1804350116/-DCSupplemental.

sediment would be large. Using generally conservative estimates for average crust and mantle ϵ_{Hf} and continental magmatic flux, we calculate (*Materials and Methods*) that the observed Hf isotope excursion would suggest the recycling of some $2.4 \times 10^8 \text{ km}^3$ of average crust, corresponding to the erosion of 1.6 km of crust globally if distributed evenly across the continents. Accounting for the low recycling efficiency of subducted Hf into new arc magmas—which is poorly known but likely less than 50%, considering the immobility of Hf in slab fluids (33)—would suggest even larger volumes of subducted crust, $\sim 3.2 \text{ km}$ or greater.

Neoproterozoic Glaciation and Erosion

Erosional unconformities are common throughout the geologic record and often have a plausible tectonic cause. The same could be said locally for specific exposures of the Great Unconformity (6). However, it is unclear how any local tectonic explanation could produce the observed global variations in preserved sediment abundance (Fig. 1) or crustal recycling (Fig. 2). Neoproterozoic glacial erosion (34) provides a simple mechanism which may reconcile rapid global erosion and sediment subduction with the constraints of the sedimentary record. Glaciers are unique among erosive agents in their ability to alter erosive base level: Glaciation promotes continental denudation both indirectly by lowering global sea level (exposing the continents to subaerial erosion) and directly through subglacial erosion. While rates are variable, in the presence of a large topographic gradient modern subglacial erosion has proved sufficiently erosive to effectively limit global mountain height, evidently outstripping tectonic uplift rates on the order of kilometers per million years (35).

Continental glaciation extended to low paleolatitudes in three well-established Neoproterozoic intervals: the Sturtian (717–660 Ma), Marinoan (641–635 Ma), and Gaskiers ($\sim 580 \text{ Ma}$)—the first two envisioned as global “snowball” events (36, 37) and the Gaskiers as an extensive, but not pan-glacial, event (38). While ice sheet thickness on a snowball Earth is imperfectly constrained and likely heterogeneous (0–6 km) (39–41), glaciation on all continents analogous to that currently found in Antarctica ($\sim 2 \text{ km}$ average thickness) would lower sea level by $\sim 787 \text{ m}$ before isostatic adjustment. After isostatic and local gravitational adjustments, modeled freeboard for ice-covered Neoproterozoic continents is variable but positive, with global averages of 400–650 m for each glacial episode (39). Moreover, if not otherwise constrained by air or water temperature, ice base level may extend up to 0.89 km below sea level per kilometer of ice sheet thickness. Such a configuration would provide a large gravitational potential energy gradient to drive erosion, while isostatically permitting more than 12 km of vertical erosion of typical continental crust by a 2-km ice sheet.

The extent of ice-free ocean available to sustain hydrological cycling during such global glaciation is controversial (41, 44). However, precipitation rates driven by sublimation alone appear sufficient for the development of localized wet-based ice streams with high basal sliding velocities and consequent erosive potential (40); evaporation from cryoconite ponds [a notable sink for solar radiation in a snowball state (45)] might further enhance hydrological cycling. Much of the characteristic field evidence for Neoproterozoic glaciation is unmistakably erosional, including striated pavements, striated and exotic clasts and dropstones, and preserved glacial diamictites (36, 46, 47). Although not always well exposed, direct unconformable contact between Neoproterozoic glacial sediments and Archean to Neoproterozoic crystalline basement may be found on most continents (48).

While the Great Unconformity surface in Fig. 1*B* allows some $\sim 0.9 \text{ Gy}$ for exhumation of crystalline basement to the surface, other sections may be found where a basement unconformity directly superposes Neoproterozoic glacial diamictites

with crystalline basement only some tens to hundreds of million years older. In the Mirbat region of Oman, for instance, Sturtian glacial diamictites and syn-glacial sediments unconformably overlie a juvenile crystalline basement complex with ages ranging from $\sim 810 \text{ Ma}$ to as young as $696.7 \pm 0.5 \text{ Ma}$ (49–51), raising the possibility of exhumation of syn-Sturtian phaneritic igneous rocks to the surface during the glacial episode. In sections with less exceptional preservation, juvenile clasts in Neoproterozoic diamict may provide additional evidence for direct glacial erosion of young crystalline basement: For instance, Sturtian glacial deposits of the Rapitan Group contain granitic basement clasts as young as $755 \pm 18 \text{ Ma}$ (52). Since exploitation of a gravitational potential energy gradient facilitates rapid glacial erosion (35), glacial erosion of young basement may be concentrated in areas of preexisting topography. Critically, Neoproterozoic glacial erosion need not be spatially uniform to produce the observed sediment subduction signature—nor should we expect uniform glacial erosion considering the negligible erosional potential of cold-based ice, the localized erosion of outlet ice streams, and the preservation (often in areas of tectonic subsidence) of relatively complete sections lacking appreciable glacial erosion (e.g., ref. 53).

Modern glacial erosion rates are highly variable, estimated to span some four orders of magnitude from $\sim 0.01 \text{ mm/y}$ to $\sim 100 \text{ mm/y}$ (54). For comparison, 4 km of erosion over 64 Ma of Neoproterozoic glaciation would require an average erosion rate of only 0.0625 mm/y —nearly two orders of magnitude slower than recent direct estimates for the modern Greenland ice sheet (55); while some such estimates (if reversible processes are involved) must be corrected for timescale dependence, the required rate is nonetheless well within the range of physical feasibility for glacial erosion. Moreover, while Sturtian and Marinoan glacial deposits evidence accumulation rates 3–10 times slower than modern equivalents (45, 56), accommodation space—not depositional process or sediment supply—is likely the rate-limiting variable at applicable ($>5 \text{ My}$) timescales (56); in the absence of such accommodation, sediment will not accumulate on the continents, but rather in the ocean basins below erosional base level. Consistent with an accommodation-limited model, Neoproterozoic diamictites may reach kilometer-scale thicknesses where directly accommodated by local syndepositional tectonism (46, 47). In the context of global glaciation, accommodation must be considered as a competition between subsidence and regional upland erosion: Local thermal or tectonic subsidence may be thwarted by isostatic rebound from regional erosion (*SI Appendix, Fig. S11*).

Delivery of eroded sediment to the deep ocean basins is a critical requirement for the production of the observed Great Unconformity (where much of the eroded crust is not found elsewhere on the continents) and is consistent with predictions for Neoproterozoic glacial erosion. During pan-glacial conditions, the locus of deposition should shift to deeper waters as a result of (i) lowered erosional base level; (ii) direct transport of eroded sediment by erosive outlet glaciers [such as those responsible for the Chuos paleovalley (47)], which in the present day are often associated with overdeepened fjords that extend to the edge of the continental shelf; and (iii) settling of fine glacial flour in deep ocean basins. In more simplistic terms, when all continental area is below ice base level during a snowball glaciation, most sediment is transported entirely off the continental shelves and into the ocean basins, where it is ultimately subducted—just as suggested by the observed Hf and O isotope records (Fig. 2).

Direct and indirect implications are widespread when considering a geological event as nonuniformitarian as the proposed kilometer-scale Cryogenian erosion, resulting in numerous testable predictions. For instance, crust exhumed by large-scale erosion cools as thermal diffusion adjusts to the new relative position of the surficial boundary condition. A range of existing

thermochronologic inversions, although geographically variable, appear permissively consistent with $\sim 100\text{--}300\text{ }^{\circ}\text{C}$ ($\sim 3\text{--}9\text{ km}$ at a $33\text{ }^{\circ}\text{C}/\text{km}$ geothermal gradient) of potentially rapid Neoproterozoic crustal exhumation (57–60). Further analyses are required to conduct a systematic global survey of the long-term thermal history of the continents, since a large proportion of existing thermochronologic data is focused on areas of more recent tectonic activity that are unlikely to preserve a record of Neoproterozoic exhumation.

One specific testable prediction concerns the terrestrial bolide impact record: Impact craters are surficial features, subject to destruction by exhumation and erosion. Since impact craters are shallow relative to their diameter, kilometer-scale Neoproterozoic erosion, if widespread, should significantly reduce the preservation potential of all but the largest impact craters. Fig. 3A shows the record of known terrestrial impact craters larger than 10 km diameter with ages known within $\pm 75\text{ My}$, updated from the Planetary and Space Science Center (PASSC) compilation (42). While the abundance of $>10\text{-km}$ impact craters closely follows exposed bedrock area for the past 700 My, only

two craters matching the criteria of Fig. 3 predate the onset of Sturtian glaciation, both deeply eroded remnants of massive craters: Sudbury and Vredefort, eroded to depths of 4.2–5.8 km and 8–11 km, respectively (61, 62). This trend is particularly striking when considered as a function of crater density per unit area (Fig. 3A and *SI Appendix*, Fig. S12), with an abrupt truncation of $<100\text{-km}$ diameter craters before 700 Ma and $<10\text{-km}$ diameter craters before 600 Ma—temporally consistent with progressive Neoproterozoic glacial erosion.

More qualitatively, we may extend our analysis of preservational bias from the bolide impact record to consider a wide range of geological features with an affinity for the shallow crust. For instance, we may predict that any mineral assemblage which cannot survive prolonged low-grade metamorphism in a normal continental geotherm should be less abundant before the Sturtian. This prediction appears consistent with the noted absence of thermodynamically fragile (U)HP/LT assemblages such as jadeitites and glaucophane eclogites before $\sim 700\text{ Ma}$ (63, 64), although not uniquely so (65, 66). The same prediction appears likewise consistent with the strong (and apparently stepwise) “preservational bias toward [mineral] deposits of the Phanerozoic Eon” reported by Liu et al. (page 2 in ref. 19).

Consequences of Rapid Crustal Erosion

The timing of Neoproterozoic glaciation is remarkably consistent with both the observed zircon isotopic excursions and continental sediment coverage history at the scale of Fig. 2. This discontinuous record is an expected consequence of the stepwise preservation potential imposed by focusing extensive, if nonuniform, kilometer-scale continental denudation into a few discrete episodes of intense glacial erosion amid a background of comparatively negligible ($<2.5\text{ m}/\text{My}$) cratonic exhumation (67). Consequently, the observed sediment coverage record may be considered in part a discretization of the exponential survivorship curve (10) that would result from continuous erosion (e.g., *SI Appendix*, Fig. S4).

In this discretization, each glacial epoch acts as a filter in the crustal record, removing some proportion of older sediments via erosion. Since erosional surfaces are subject to capture by subsequent erosion, the most dramatic unconformity (and largest step in preserved sediment abundance) may be inherited by the most recent glaciation, consistent with Fig. 2E. However, such erosion does not preclude a constructive contribution to the Great Unconformity; to the contrary, it requires one. Continental thinning through erosion directly decreases continental freeboard, raising relative sea level and providing accommodation space for sediment accumulation. While this new accommodation space may be temporarily moderated by thermal buoyancy given erosional advection of the continental geotherm, continental erosion nonetheless inevitably leads to increased continental sediment storage, as proposed by ref. 8.

To quantify the depositional consequences of rapid Neoproterozoic erosion, we constructed a 1D model of continental freeboard, combining the effects of erosion, isostasy, thermal subsidence, and sediment accumulation over the past 800 My. Using either the Phanerozoic net sedimentation rate from Fig. 1A or a constant assumed rate of $0.9\text{ km}^3/\text{y}$, varying the model magnitude of Neoproterozoic erosion directly influences initial freeboard via mass balance (*SI Appendix*, Fig. S13). Near-modern freeboard at 750 Ma is reproduced with 3.4–4.5 km Neoproterozoic glacial erosion, producing in each case a nearly 250-m isostatic excursion in relative sea level (Fig. 4A). Using a modern hypsometric profile (*SI Appendix*, Fig. S15) to convert from sea level to continental submergence fraction as illustrated in Fig. 4B, this 250-m excursion corresponds remarkably well with the observed macrostratigraphic record of marine sediment coverage.

The first-order success of this 1D freeboard model prediction is particularly remarkable considering that the model includes no

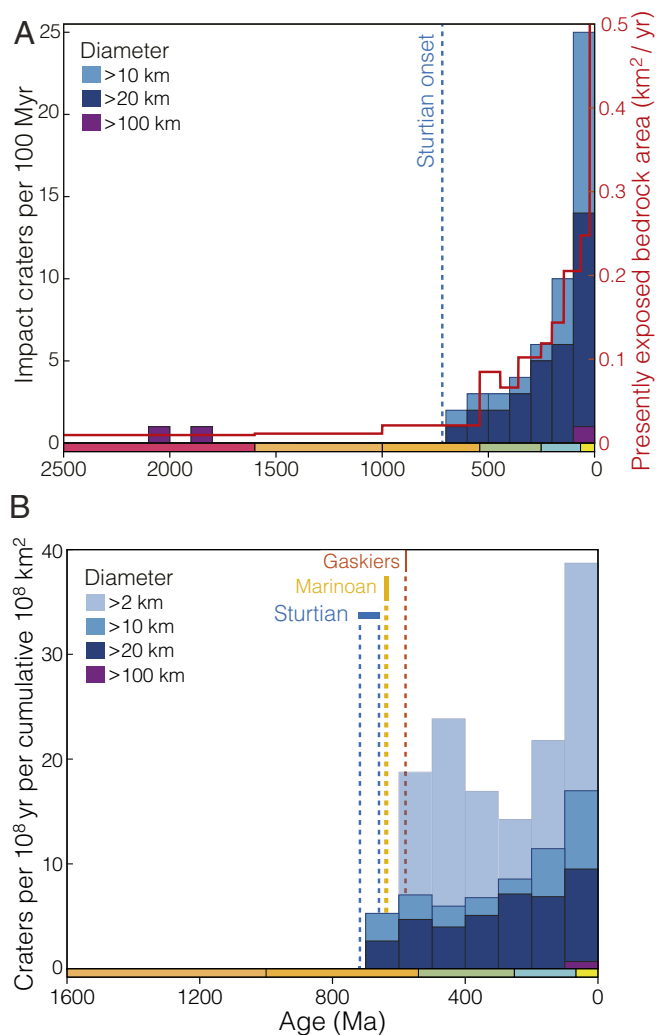


Fig. 3. The record of impact craters preserved in Earth's continental crust with formation ages known to within $\pm 75\text{ My}$ ($1\text{-}\sigma$) from the PASSC database (42). (A) Absolute crater counts (left axis) for several size ranges tallied in 100-My bins over the past 2.5 Ga, plotted alongside global exposed bedrock area in km^2/y (right axis) (43). (B) Apparent impact cratering rate per unit bedrock area area tallied in 100-My bins for crater diameters from 2 km to $>100\text{ km}$.

Proterozoic or Archean basement is commonly exposed at the surface even today (Fig. 5)—an ongoing Great Unconformity. However, exhumation at such sites likely results from multiple ancient (e.g., Neoproterozoic) unconformities collapsed, captured, and deepened by more recent erosion. A remarkable correspondence has been noted between Precambrian bedrock exposure and glaciation (Fig. 5); virtually all nonorogenic exposures of Precambrian basement have been subject to glaciation during either the Late Paleozoic Ice Age or the Quaternary (73, 81) (*SI Appendix, Fig. S16*). In this context, we suggest that the present icehouse epoch may display comparatively high continental erosion rates (82) relative to the Phanerozoic background, reconciling unsustainable modern erosion rates of 0.05–0.5 mm/y (i.e., 50–500 km/Gy) with the survival of Archean crust and lithosphere (67).

Considering the glacial model for the Great Unconformity proposed here, zircon Hf and O isotopes may represent the first paleoerosion proxy preserved in Earth's igneous record, preserving a signal of surface earth processes over billion-year timescales. In this context, we note that a set of smaller but correlated Paleoproterozoic excursions in the zircon Hf and O isotope records circa 2.2 Ga appears following a known period of Paleoproterozoic glaciation (83). Given the lack of geologic evidence for glacial deposits between the ~2.2-Ga Rietfontein (83) and ~0.72-Ga Sturtian (37) glaciations, Earth may have experienced a prolonged period of weathering and regolith development (84) with comparatively little marine sediment accumulation on the continents due to a lack of glaciation-derived accommodation space. Thus, Neoproterozoic global glaciation may have been responsible for initiating a Phanerozoic cycle of continental sedimentation with enhanced Paleozoic continental inundation and sediment accumulation relative to the preceding late Proterozoic. We conclude that the Phanerozoic sedimentary record is best explained by a Great Unconformity of inherently coupled erosive and constructive genesis, with Neoproterozoic glacial erosion governing the subsequent history of continental freeboard and sediment accumulation (Fig. 4B). As such, the environmental and geochemical changes that led to the diversification of multicellular animals (5) may be considered a direct consequence of Neoproterozoic glaciation.

Materials and Methods

To investigate anomalies in the continental rock record near the Proterozoic–Phanerozoic boundary, we assemble a range of stratigraphic, geochemical, and geological datasets. Stratigraphic data for North America are obtained from the Macrostrat database (macrostrat.org), originally produced by Peters (7) by digitization of the the American Association of Petroleum Geologists Correlation of Stratigraphic Units of North America (COSUNA) charts (85). This stratigraphic record of the Great Unconformity is interpreted alongside compiled zircon Hf and O isotope geochemistry, as well as terrestrial and lunar bolide impact datasets. Finally, stratigraphic and geochemical results are integrated and interpreted in the context of an isostatic and thermal model of continental freeboard. Computational source code and data are freely available at <https://github.com/brenhinkeller/GreatUnconformity>.

Zircon Isotope Systematics and Monte Carlo Analysis. We compiled zircon Hf and O isotopic compositions along with U–Pb ages for igneous and detrital zircons from the preexisting datasets of Belousova et al. (86), Dhume et al. (87), and Spencer et al. (88)/Payne et al. (89), augmented by some further compilation of literature data, resulting in a dataset of 35,368 analyses from all continents (*SI Appendix, Figs. S5 and S6*), of which 29,523 are unique. To obtain a maximally representative temporal record of zircon Hf and O isotopic composition, we applied weighted-bootstrap resampling following the approach of Keller and Schoene (13, 16). While ages are known directly for each analysis, geographic locations are largely absent from the dataset. Consequently, sample weights w_i for each sample i are assigned inversely proportional to temporal sample density following the relation

$$w_i = 1 / \sum_{j=1}^n \frac{1}{(t_i - t_j)^2 + 1},$$

where n is the number of samples in the dataset and t is sample age. Subsequently, the dataset is resampled with replacement, with sampling probability proportional to sample weight. This weighting produces a more even temporal distribution (*SI Appendix, Fig. S7*) and obviates the manual elimination of, e.g., duplicate analyses. Throughout resampling, each geochemical measurement (e.g., a single zircon Hf isotope ratio) is represented as a Gaussian random variable with a known mean and SD such that a new value is drawn from this distribution each time the dataset is resampled, thereby fully representing analytical uncertainty. Average results throughout Earth's history are presented as an average and 2 SE of the mean for overlapping 90-Ma windows between 0 Ma and 4,350 Ma (e.g., Fig. 2).

The global average zircon Hf and O isotope timeseries both record the recycling of preexisting crust into new magmas. Positive O isotope excursions above the mantle baseline (~5.5‰) reflect the recycling of silicate crust that has undergone low-temperature aqueous alteration at Earth's surface (i.e., sediment), while negative Hf isotope excursions reflect the recycling of old, felsic crust that has undergone less ^{176}Hf ingrowth than the convecting mantle. Zircon Hf and O isotope averages vary throughout the supercontinent cycle as the proportion and preservation of arc, rift, and collisional magmatism vary (29–31); such normal variations are observed throughout the entirety of the preserved record, with roughly the expected periodicity (*SI Appendix, Fig. S10*). Compared with this normal tectonic background, the Neoproterozoic excursions are notable both in magnitude and in the covariance between Hf and O isotope records. While atypical O and Hf isotope characteristics of Neoproterozoic zircon have been previously noted (30, 31, 90), their systematic global covariance and the broader implications thereof have not been previously explored.

To assess the importance of sediment subduction, we examined the covariance between the zircon Hf isotope signature of felsic crustal recycling and the zircon O isotope signature of sediment recycling, following a procedure illustrated in *SI Appendix, Fig. S9*. First, to remove any scale dependence or extraneous covariance from long-term secular crustal evolution (as opposed to distinct crustal recycling episodes), both isotopic records are detrended and normalized to unit variance, with the εHf isotopic signal inverted such that increasing recycling is positive for both systems (*SI Appendix, Fig. S9 A and B*). The resulting covariance is illustrated in *SI Appendix, Fig. S9C*. This raw covariance is positive where the Hf and O signals either increase or decrease in concert: Both the excursion and recovery of the Neoproterozoic isotope anomaly yield large positive covariance peaks. Since we wish to distinguish between excursion (increasing sediment subduction) and recovery (decreasing sediment subduction back to baseline), we additionally examine the product of this covariance with the average slope of the two Hf and O isotope signals (*SI Appendix, Fig. S9D*). Since the average slope tends to zero in the case of negative covariance, the covariance–slope product (*SI Appendix, Fig. S9E*) emphasizes large positive covariance co-occurring with either increasing or decreasing sediment subduction; individual subduction events thus appear as characteristic pairwise features with a positive excursion peak immediately followed by a negative recovery peak. Two such events are evident: a Paleoproterozoic pair with an excursion beginning circa 2,200 Ma and a much larger Neoproterozoic pair with an initial excursion coincident with the onset of the Sturtian glaciation [~ 717 Ma (37, 91)], a nadir at ~ 560 Ma, and an ~ 220 -My recovery that is complete by ~ 340 Ma. Notably, the essentially immediate (on gigayear scales) onset of the excursion following Sturtian glaciation is consistent with the fast recycling of sediment into new magmas (< 7 –9 Ma from erosion to eruption) suggested by cosmogenic ^{10}Be anomalies in modern arc magmas (92)—while the timescale of recovery is entirely consistent with the ~ 200 -My characteristic timescale for complete turnover of the oceanic crust (and thus complete subduction of any accumulated sediments into the ocean basins).

Given the observed magnitude of the global Hf isotope excursion, we may estimate the minimum required volume of subducted crust. Taking the compiled zircon εHf dataset as an estimate of average εHf of new igneous crust throughout Earth's history, we may calculate the average crustal εHf at any subsequent time accounting for Hf ingrowth in accordance with Lu/Hf ratios for each whole-rock sample in the dataset of Keller and Schoene (13), obtaining Neoproterozoic values ranging from -33.7ε at 717 Ma to -34.9ε at 635 Ma. Since a more negative crustal endmember will result in lower estimated volume of subducted crust, we choose -35ε as a minimum value. This estimate is conservative since the zircon record samples only zircon-bearing magmas, which are predominantly felsic (26) and may exhibit more negative initial εHf than average crust due to a greater contribution from assimilation of preexisting crust than, e.g., a primitive basalt. Meanwhile, as the most positive reservoir in εHf space, the evolution of the depleted mantle may be traced as the upper limit of the compiled εHf field through time,

estimating a value of $+14\epsilon$ for the Neoproterozoic (*SI Appendix, Fig. S6*). As seen in Fig. 2, the Neoproterozoic negative ϵ_{Hf} excursion ranges from a baseline of $+4\epsilon$ to a nadir of -8ϵ , with a depth of 12ϵ , with an average depth of 5.7ϵ over the 400-My duration of the excursion. This average depth corresponds to $5.7/(14 - (-35)) = 0.12$ of the total range between average crust and depleted mantle, equivalent to shifting 12% of total continental magmatism over the duration of the excursion from a mantle source to a crustal source.

Phanerozoic estimates of rates of volcanic and plutonic magmatism in the continental crust suggest 3–8 km³/y of arc volcanism and plutonism along with 0.2–1.5 km³ of intraplate continental magmatism (93). More recent mass balance constraints suggest at least 3.8 km³/y of arc magmatism is required to avoid long-term crustal destruction. Consequently, we take 5 km³/y as a relatively conservative estimate of total continental magmatism. In this case, shifting 12% of continental magmatism from a mantle source to a crustal source over 400 My would require the recycling of some 2.4×10^8 km³ of average crust. Such a volume corresponds to 1.61 vertical kilometers if distributed evenly over the 1.489×10^8 km² area of the continents. Considering that only a fraction of subducted Hf makes its way into new magmas (depletion of high-field-strength elements such as Hf is a characteristic signature of arc magmatism due to the immobility of these elements in aqueous slab fluids) (33), the true value is likely at least twice that, or $\sim 5 \times 10^8$ km³ if this recycling occurs via sediment subduction.

The Terrestrial Bolide Impact Record. To obtain an independent constraint on the timing and magnitude of Neoproterozoic erosion, we have examined the terrestrial impact crater record as compiled in the PASSC Earth Impact Database (42), with age constraints updated where applicable. Since bolide impact craters necessarily occur at Earth's surface, their resistance to erosion is a function of crater depth. Hypervelocity impact craters are characteristically shallow features, with an initial depth around 1/10th of their original diameter or less (94, 95), decreasing above 15 km diameter such that a Lunar impact crater of 100 km diameter may be only 4 km deep (95). Consequently, all but the largest terrestrial impact craters should be susceptible to erasure by Neoproterozoic glacial erosion. If the Neoproterozoic glacial erosion hypothesis is correct, we expect a dramatic decrease in impact crater preservation potential across the Cryogenian for all but the largest class of terrestrial impacts. While this prediction is broadly confirmed by the raw impact record alone (Fig. 3A), the signal of preservation is better resolved by normalizing the impact record to the continental area that was available for impact cratering at some time in the past and is now again exposed at the surface.

We explore two such normalizations, (i) to the cumulative area of crust exposed today that is older than a given impact age and (ii) to the surface area of crust exposed today of the same age as a given impact crater (*SI Appendix, Fig. S12 A and B*). The first normalization (by cumulative exposed area, as seen in Fig. 3B and *SI Appendix, Fig. S12D*) is the most conservative in that the presently exposed area bedrock of age X Ma or greater is the maximum exposed surface area that could preserve an impact of age X Ma. This is a maximum extent because, for instance, 1-Ga bedrock may be extant at 0.5 Ga, but deeply buried and thus unable to record an impact at that time.

The latter normalization (by the relative area of exposed crust of the same age as a given impact, within some binning resolution) is more aggressive but may be considered more natural for sedimentary or volcanic bedrock, which must have been exposed at the time of deposition and thus would have been available as a target for bolide impacts at that time. This normalization results in an even more dramatic discontinuity in preserved cratering rate across the Cryogenian (*SI Appendix, Fig. S12C*). The true preservation signal is likely intermediate between *SI Appendix, Fig. S12 C and D*, but in either scenario strikingly lower preservation potential is suggested for impact craters predating Neoproterozoic glaciation.

Continental Freeboard and the Sedimentary Record. The Great Unconformity is manifest in the macrostratigraphic record of continental sedimentation in the form of a series of approximately stepwise increases in preserved sediment abundance between approximately ~ 720 Ma and ~ 500 Ma (Figs. 2E and 4). In an erosional context, each step may be considered to reflect a decreasing probability of any preexisting sediment having survived past a given glacial episode. For instance, sediments older than the Gaskiers may have survived only one Neoproterozoic glaciation, while sediments older than the Sturtian must have survived all three. Moreover, since erosive glaciation tends to capture the evidence of previous erosion, the largest abundance step (and most dramatic unconformity) may be inherited by the most recent glaciation, consistent with the results of Fig. 2E. For instance,

if the Sturtian and Marinoan together were to erode 3 km of crust, followed by 100 m of sedimentation between 635 Ma and 580 Ma, the Gaskiers need only erode 100 m of sediment to capture the entire (now) 3.1-km unconformity.

To quantify the consequences of Neoproterozoic erosion for continental freeboard and sediment accumulation, we constructed a 1D thermal and isostatic model of the continental crust and lithosphere. On approximately gigayear simulation timescales, isostatic adjustment is assumed to be effectively instantaneous, with postglacial viscous mantle rebound (45, 96) likely complete within a single-million-year model timestep. However, the thermal consequences of kilometer-scale erosion may be more protracted. To account for thermal subsidence as the advected geotherm decays back into equilibrium, along with the direct isostatic effects of erosion and sedimentation, our model assumes a coefficient of thermal expansion of $3 \times 10^{-5}/\text{K}$, a thermal diffusivity of 1 mm²/s, an average crustal thickness of 33 km, an average density of 2,818 kg/m³ for the continental crust (97), a mantle density of 3,300 kg/m³, and a slightly buoyant mantle lithosphere (3,250 kg/m³) of 100-km thickness, for a total lithospheric thickness (crust + mantle lithosphere) of 133 km, generally intermediate between expected thermal (98) and elastic (96) lithospheric thicknesses. This model was then perturbed by various scenarios of erosion and sedimentation, with several kilometers of Neoproterozoic erosion followed by either continuous (0.9 km³/y) or variable (Macrostrat derived, as in Fig. 1A) sedimentation rate. For the purposes of Fig. 4 and *SI Appendix, Fig. S13*, the total volume of glacial erosion was partitioned between the three Neoproterozoic glacial intervals in proportion to their duration. However, instead of equally distributing erosion between all three glaciations has little impact on the results (*SI Appendix, Fig. S14*).

To better understand the implications of this model for continental emergence and sedimentation, the resulting freeboard curve was translated into expected continental coverage extent, using a present-day hypsometric curve (*SI Appendix, Fig. S15*). The assumption of present-day hypsometry is notably imperfect, but presently unavoidable given an absence of independent constraints on past global hypsometry. Glaciation may significantly alter continental hypsometry—with the potential to either produce or destroy topographic contrast under different conditions (71). Consequently, the global hypsometric gradient is poorly constrained both before and in the immediate aftermath of Neoproterozoic glaciation. The assumption of near-modern hypsometry is more supportable closer to the present day (i.e., the past 500 My), which is perhaps unsurprisingly where model misfit is lower.

As illustrated in Fig. 4, the model results are remarkably consistent with the observed continental coverage extent curve, with continental coverage increasing dramatically in the aftermath of Neoproterozoic erosion and then slowly declining to background as continued sedimentation fills the available accommodation space. While the general agreement between model and observed coverage trends is quite good given the wide range of uncertainties involved, two particular intervals of misfit are apparent: (i) a period in the middle Cretaceous where observed coverage substantially exceeds model expectations and (ii) systematically lower than expected coverage before ~ 500 Ma.

A wide range of factors may introduce such misfit. First, no specific tectonic or orogenic events are included in our simple 1D model. In this context, the relatively low misfit after ~ 500 Ma is arguably surprising and suggests that the global rates of relevant local processes such as orogenesis and basin formation may not have varied wildly over the past 500 My. Systematic variation in mantle heat flow may change oceanic spreading rate (99) and midocean ridge height, thus changing average global sea level. Additional misfit may be introduced by erosional or nondepositional unconformity in the record subsequent to the initial Great Unconformity; continental emergence will be overestimated if we are missing the sediments by which we estimate coverage. Any change in the form of the terrestrial hypsometric profile between 800 Ma and today—likely, but difficult to test—would introduce error into the function mapping between continental freeboard and coverage extent. Finally, the accuracy of the observed coverage record is entirely dependent on the accuracy of the underlying geochronological constraints.

One might at first consider this Cretaceous anomaly as a regional bias reflecting the well-known Cretaceous Interior Seaway of North America (100, 101) attributable to, e.g., regional tectonics or dynamic topography. However, the Cretaceous has long been known as a time of anomalous flooding on multiple continents (102), and indeed a positive coverage anomaly is observed even in the coarser-timescale global record of Ronov (23) as seen in Fig. 4B. Consequently, this excursion may be more consistent with a global increase in midocean ridge elevation and spreading

rate. While controversial, increased mantle heat flow in the Cretaceous has been proposed in conjunction with the Cretaceous Long Normal Superchron and the Kerguelen and Ontong–Java oceanic flood basalt plateau (103–105), potentially consistent with high average ocean ridge elevation and increased sea level for much of the Cretaceous.

Code and Data Availability. Macrostratigraphic data are accessible via <https://macrostrat.org/api>. All compiled datasets and computational source code are available at <https://github.com/brenhinkeller/GreatUnconformity>.

- Powell JW, Thompson AH, Coues E, Goode GB (1875) *Exploration of the Colorado River of the West and its Tributaries* (Government Printing Office, Washington, DC).
- Walcott CD (1914) *Cambrian Geology and Paleontology*, Smithsonian Miscellaneous Contributions (The Lord Baltimore Press, Washington, DC), Vol 57.
- Sloss LL (1963) Sequences in the cratonic interior of North America. *Geol Soc Am Bull* 74:93–114.
- Ronov AB, Khain VE, Balukhovskiy AN, Seslavinsky KB (1980) Quantitative analysis of Phanerozoic sedimentation. *Sediment Geol* 25:311–325.
- Peters SE, Gaines RR (2012) Formation of the ‘Great Unconformity’ as a trigger for the Cambrian explosion. *Nature* 484:363–366.
- Karlstrom KE, Timmons JM (2012) Many unconformities make one ‘Great Unconformity’. *Grand Canyon Geology: Two Billion Years of Earth’s History*, eds Timmons JM, Karlstrom KE (Geol Soc Am, Boulder City, CO), GSA Special Paper 489, pp 73–79.
- Peters SE (2006) Macrostratigraphy of North America. *J Geol* 114:391–412.
- Husson JM, Peters SE (2017) Atmospheric oxygenation driven by unsteady growth of the continental sedimentary reservoir. *Earth Planet Sci Lett* 460:68–75.
- Peters SE, Husson JM (2017) Sediment cycling on continental and oceanic crust. *Geology* 45:323–326.
- Gregor B (1970) Denudation of the continents. *Nature* 228:273–275.
- Husson JM, Peters SE (2018) Nature of the sedimentary rock record and its implications for Earth system evolution. *Emerging Top Life Sci* 2:125–136.
- Hunter RA, Andronicos CL (2012) Deformation assisted phase transformation: An example from the sillimanite-in isograd, Eolus batholith, Needle Mountains, Colorado, USA. *Terra Nova* 25:48–56.
- Keller CB, Schoene B (2012) Statistical geochemistry reveals disruption in secular lithospheric evolution about 2.5 Gyr ago. *Nature* 485:490–493.
- Condie KC, Aster RC, van Hunen J (2016) A great thermal divergence in the mantle beginning 2.5 Ga: Geochemical constraints from greenstone basalts and komatiites. *Geosci Front* 7:543–553.
- Ganne J, Feng X (2017) Primary magmas and mantle temperatures through time. *Geochim Geophys Geosyst* 18:872–888.
- Keller CB, Schoene B (2018) Plate tectonics and continental basaltic geochemistry throughout Earth history. *Earth Planet Sci Lett* 481:290–304.
- Murphy JB, Nance RD (2003) Do supercontinents introvert or extrovert?: Sm–Nd isotope evidence. *Geology* 31:873–876.
- Cawood PA, Hawkesworth CJ (2014) Earth’s middle age. *Geology* 42:503–506.
- Liu C, Knoll AH, Hazen RM (2017) Geochemical and mineralogical evidence that Rodinia assembly was unique. *Nat Commun* 8:1950.
- Dietz RS (1961) Continent and ocean basin evolution by spreading of the sea floor. *Nature* 190:854–857.
- Clift PD, Vannucchi P, Morgan JP (2009) Crustal redistribution, crust–mantle recycling and Phanerozoic evolution of the continental crust. *Earth-Sci Rev* 97: 80–104.
- Jagoutz O, Kelemen PB (2015) Role of arc processes in the formation of continental crust. *Annu Rev Earth Planet Sci* 43:363–404.
- Ronov AB (1994) Phanerozoic transgressions and regressions on the continents: A quantitative approach based on areas flooded by the sea and areas of marine and continental deposition. *Am J Sci* 294:777–801.
- Bouvier A, Vervoort JD, Patchett PJ (2008) The Lu–Hf and Sm–Nd isotopic composition of CHUR: Constraints from unequilibrated chondrites and implications for the bulk composition of terrestrial planets. *Earth Planet Sci Lett* 273:48–57.
- Cherniak DJ (2003) Diffusion in zircon. *Rev Mineral Geochem* 53:113–143.
- Keller CB, Boehnke P, Schoene B (2017) Temporal variation in relative zircon abundance throughout Earth history. *Geochem Perspect Lett* 3:179–189.
- Cao W, Lee CTA, Lackey JS (2017) Episodic nature of continental arc activity since 750 Ma: A global compilation. *Earth Planet Sci Lett* 461:85–95.
- Keller CB, Schoene B, Barboni M, Samperton KM, Husson JM (2015) Volcanic–plutonic parity and the differentiation of the continental crust. *Nature* 523:301–307.
- Iizuka T, Yamaguchi T, Itano K, Hibiya Y, Suzuki K (2017) What Hf isotopes in zircon tell us about crust–mantle evolution. *Lithos* 274–275:304–327.
- Spencer CJ, Hawkesworth C, Cawood PA, Dhruve B (2013) Not all supercontinents are created equal: Gondwana–Rodinia case study. *Geology* 41:795–798.
- Gardiner NJ, Kirkland CL, Van Kranendonk MJ (2016) The juvenile Hafnium isotope signal as a record of supercontinent cycles. *Sci Rep* 6:38503.
- Hopkinson TN, et al. (2017) The identification and significance of pure sediment-derived granites. *Earth Planet Sci Lett* 467:57–63.
- Perfit MR, Gust DA, Bence AE, Arculus RJ, Taylor SR (1980) Chemical characteristics of island-arc basalts: Implications for mantle sources. *Chem Geol* 30:227–256.
- White WA (1973) Deep erosion by infracambrian ice sheets. *Geol Soc Am Bull* 84:1841–1844.
- Egholm DL, Nielsen SB, Pedersen VK, Lesemann JE (2009) Glacial effects limiting mountain height. *Nature* 460:884–887.
- Hoffman PF, Li ZX (2009) A palaeogeographic context for Neoproterozoic glaciation. *Palaeogeogr Palaeoclimatol Palaeoecol* 277:158–172.
- Rooney AD, Strauss JV, Brandon AD, Macdonald FA (2015) A Cryogenian chronology: Two long-lasting synchronous Neoproterozoic glaciations. *Geology* 43:459–462.
- Pu JP, et al. (2016) Dodging snowballs: Geochronology of the Gaskiers glaciation and the first appearance of the Ediacaran biota. *Geology* 44:955–958.
- Liu Y, Peltier WR (2013) Sea level variations during snowball Earth formation: 1. A preliminary analysis. *J Geophys Res Solid Earth* 118:4410–4424.
- Donnadieu Y, Fluteau F, Ramstein G, Ritz C (2003) Is there a conflict between the Neoproterozoic glacial deposits and the snowball Earth interpretation: An improved understanding with numerical modeling. *Earth Planet Sci Lett* 208:101–112.
- Hyde WT, Crowley TJ, Baum SK, Peltier WR (2000) Neoproterozoic ‘snowball Earth’ simulations with a coupled climate/ice-sheet model. *Nature* 405:425–429.
- PASSC (2001) *Earth Impact Database* (The Planetary and Space Science Centre, Fredericton, New Brunswick, Canada).
- Geological Survey of Canada (1995) Generalized geological map of the world and linked databases (Geological Survey of Canada, Ottawa, Ontario, Canada), Technical Report 2915d.
- Pollard D, Kasting JF, Zuger ME (2017) Snowball Earth: Asynchronous coupling of sea-glacier flow with a global climate model. *J Geophys Res Atmos* 122:5157–5171.
- Hoffman PF, et al. (2017) Snowball Earth climate dynamics and Cryogenian geology-geobiology. *Sci Adv* 3:e1600983.
- McMechan ME (2000) Vreeland diamictites–Neoproterozoic glaciogenic slope deposits, Rocky Mountains, northeast British Columbia. *Bull Can Pet Geol* 48: 246–261.
- Hoffman PF, et al. (2017) Sedimentary depocenters on snowball Earth: Case studies from the Sturtian Chuos Formation in northern Namibia. *Geosphere* 13:811–837.
- Arnaud E, Halverson GP, Shields-Zhou G, eds (2011) *The Geological Record of Neoproterozoic Glaciations* (Geol Soc London, London), Geological Society Memoir No. 36.
- Rieu R, Allen PA, Etienne JL, Cozzi A, Wiechert U (2006) A Neoproterozoic glacially influenced basin margin succession and ‘atypical’ cap carbonate associated with bedrock palaeovalleys, Mirbat area, southern Oman. *Basin Res* 18:471–496.
- Bowring SA, et al. (2007) Geochronologic constraints on the chronostratigraphic framework of the Neoproterozoic Huqf Supergroup, Sultanate of Oman. *Am J Sci* 307:1097–1145.
- Rantakokko NE, Whitehouse MJ, Pease V, Windley BF (2014) Neoproterozoic evolution of the eastern Arabian basement based on a refined geochronology of the Marbat region, Sultanate of Oman. *Geol Soc Spec Publ* 392:101–127.
- Ross GM, Villeneuve ME (1997) U–Pb geochronology of stranger stones in Neoproterozoic diamictites, Canadian Cordillera: Implications for provenance and ages of deposition (Geological Survey of Canada, Ottawa, Ontario, Canada), Technical Report 1997-F.
- Rose CV, et al. (2012) Constraints on the origin and relative timing of the Trezona $\delta^{13}C$ anomaly below the end-Cryogenian glaciation. *Earth Planet Sci Lett* 319–320:241–250.
- Hallet B, Hunter L, Bogen J (1996) Rates of erosion and sediment evacuation by glaciers: A review of field data and their implications. *Global Planet Change* 12:213–235.
- Cowton T, Nienow P, Bartholomew I, Sole A, Mair D (2012) Rapid erosion beneath the Greenland ice sheet. *Geology* 40:343–346.
- Partin CA, Sadler PM (2016) Slow net sediment accumulation sets snowball Earth apart from all younger glacial episodes. *Geology* 44:1019–1022.
- Heizler MT, Harrison TM (1998) The thermal history of the New York basement determined from $40Ar/39Ar$ K-feldspar studies. *J Geophys Res Solid Earth* 103:29795–29814.
- Flowers RM, Bowring SA, Reiners PW (2006) Low long-term erosion rates and extreme continental stability documented by ancient (U–Th)/He dates. *Geology* 34:925–928.
- Karlstrom KE, Heizler M, Quigley MC (2010) Structure and $40Ar/39Ar$ K-feldspar thermal history of the Gold Butte block: Reevaluation of the tilted crustal section model. GSA Special Paper 463, eds Umhoefer PJ, Beard LS, Lamb MA (Geol Soc Am, Boulder, CO), pp 331–352.
- DeLucia MS, Guenther WR, Marshak S, Thomson SN, Ault AK (2017) Thermochronology links denudation of the Great Unconformity surface to the supercontinent cycle and snowball Earth. *Geology* 46:167–170.
- Molnar F, Watkinson DH, Jones PC (2001) Multiple hydrothermal processes in footwall units of the North Range, Sudbury Igneous Complex, Canada, and implications for the genesis of vein-type Cu–Ni–PGE deposits. *Econ Geol* 96:1645–1670.
- Gibson RL, Wu R, Stevens G (1998) Thermal-metamorphic signature of an impact event in the Vredefort dome, South Africa. *Geology* 26:787–790.
- Brown M (2006) Duality of thermal regimes is the distinctive characteristic of plate tectonics since the Neoproterozoic. *Geology* 34:961–964.

64. Harlow GE, Tsujimori T, Sorensen SS (2015) Jadeitites and plate tectonics. *Annu Rev Earth Planet Sci* 43:105–138.
65. Sizova E, Gerya T, Brown M (2014) Contrasting styles of Phanerozoic and Precambrian continental collision. *Gondwana Res* 25:522–545.
66. Palin RM, White RW (2016) Emergence of blueschists on Earth linked to secular changes in oceanic crust composition. *Nat Geosci* 9:60–64.
67. Blackburn TJ, et al. (2012) An exhumation history of continents over billion-year time scales. *Science* 335:73–76.
68. Chumakov NM (2010) Precambrian glaciations and associated biospheric events. *Stratigr Geol Correl* 18:467–479.
69. Germs GJB, Gaucher C (2012) Nature and extent of a late Ediacaran (ca. 547 Ma) glacial erosion surface in southern Africa. *S Afr J Geol* 115:91–102.
70. Chumakov NM (2011) Glacial deposits of the Bokson Group, East Sayan Mountains, Buryatian Republic, Russian Federation. *Geol Soc Lon Memoirs* 36:285–288.
71. Egholm DL, et al. (2017) Formation of plateau landscapes on glaciated continental margins. *Nat Geosci* 10:592–597.
72. Snyder FG (1947) The problem of the Liplian interval. *J Geol* 55:146–157.
73. White WA (1972) Deep erosion by continental ice sheets. *Geol Soc Am Bull* 83:1037–1056.
74. Garrity CP, Soller DR (2009) Database of the Geologic Map of North America—Adapted from the Map by J.C. Reed, Jr. and others (2005), US Geological Survey Data Series, 424. Available at <http://pubs.usgs.gov/ds/424/>. Accessed August 11, 2017.
75. Licciardi JM, Clark PU, Jenson JW, Macayeal DR (1998) Deglaciation of a soft-bedded Laurentide ice sheet. *Quat Sci Rev* 17:427–448.
76. Egged L (1956) Determination of changes in the dimensions of the Earth from Palaeogeographical data. *Nature* 178:534.
77. Armstrong RL (1969) Control of sea level relative to the continents. *Nature* 221:1042–1043.
78. Hargraves RB (1976) Precambrian geologic history. *Science* 193:363–371.
79. Lee CTA, et al. (2017) Deep mantle roots and continental emergence: Implications for whole-Earth elemental cycling, long-term climate, and the Cambrian explosion. *Int Geol Rev* 164:1–18.
80. Whitehead JA (2017) Dimensions of continents and oceans—Water has carved a perfect cistern. *Earth Planet Sci Lett* 467:18–29.
81. López-Gamundi OR, Buatois LA (2010) Introduction: Late Paleozoic glacial events and postglacial transgressions in Gondwana. GSA Special Paper 468, eds López-Gamundi OR, Buatois LA (Geol Soc Am, Boulder, CO), pp v–viii.
82. Herman F, et al. (2013) Worldwide acceleration of mountain erosion under a cooling climate. *Nature* 504:423–426.
83. Gumsley AP, Chamberlain KR (2017) Timing and tempo of the great oxidation event. *Proc Natl Acad Sci USA* 114 :1811–1816.
84. Swanson-Hysell NL, et al. (2010) Cryogenian glaciation and the onset of carbon-isotope decoupling. *Science* 328:608–611.
85. Childs OE (1985) Correlation of stratigraphic units of North America—COSUNA. *AAPG Bull* 69:173–180.
86. Belousova E, et al. (2010) The growth of the continental crust: Constraints from zircon Hf-isotope data. *Lithos* 119:457–466.
87. Dhuime B, Hawkesworth CJ, Cawood PA, Storey CD (2012) A change in the geodynamics of continental growth 3 billion years ago. *Science* 335:1334–1336.
88. Spencer CJ, et al. (2014) Proterozoic onset of crustal reworking and collisional tectonics: Reappraisal of the zircon oxygen isotope record. *Geology* 42:451–454.
89. Payne JL, et al. (2016) Strengths and limitations of zircon Lu-Hf and O isotopes in modelling crustal growth. *Lithos* 248–251:175–192.
90. Zheng YF, et al. (2004) Zircon U-Pb and oxygen isotope evidence for a large-scale 18O depletion event in igneous rocks during the Neoproterozoic. *Geochim Cosmochim Acta* 68:4145–4165.
91. MacLennan S, et al. (2018) The arc of the Snowball: U-Pb dates constrain the Islay anomaly and the initiation of the Sturtian glaciation. *Geology* 46:539–542.
92. Morris JD, Leeman WP, Tera F (1990) The subducted component in island arc lavas: Constraints from Be isotopes and B–Be systematics. *Nature* 344:31–36.
93. Crisp JA (1984) Rates of magma emplacement and volcanic output. *J Volcanol Geotherm Res* 20:177–211.
94. Smith EI (1971) Determination of origin of small lunar and terrestrial craters by depth diameter ratio. *J Geophys Res* 76:5683–5689.
95. Pike RJ (1974) Depth/diameter relations of fresh lunar craters: Revision from spacecraft data. *Geophys Res Lett* 1:291–294.
96. Lambeck K, Smither C, Johnston P (1998) Sea-level change, glacial rebound and mantle viscosity for northern Europe. *Geophys J Int* 134:102–144.
97. Laske G, Masters G, Ma Z, Pysanos M (2013) Update on CRUST1.0—A 1-degree global model of Earth's crust. *Geophys Res Abstr* 15:EGU2013-2658.
98. Artemieva IM (2006) Global 1 x 1 thermal model TC1 for the continental lithosphere: Implications for lithosphere secular evolution. *Tectonophysics* 416:245–277.
99. Larson RL (1991) Latest pulse of Earth: Evidence for a mid-Cretaceous superplume. *Geology* 19:547–550.
100. Williams GD, Stelck CR (1975) Speculations on the Cretaceous paleogeography of North America. *The Cretaceous System in the Western Interior of North America: Geological Association of Canada Special Paper*, ed Caldwell WGE (Geol Assoc Canada, Waterloo, Ontario, Canada), pp 1–20.
101. Eriksen MC, Slingerland R (1990) Numerical simulations of tidal and wind-driven circulation in the Cretaceous Interior Seaway of North America. *Geol Soc Am Bull* 102:1499–1516.
102. Hancock JM, Kauffman EG (1979) The great transgressions of the Late Cretaceous. *J Geol Soc* 136:175–186.
103. Courtillot V, Olson P (2007) Mantle plumes link magnetic superchrons to Phanerozoic mass depletion events. *Earth Planet Sci Lett* 260:495–504.
104. Tarduno JA, Cottrell RD, Smirnov AV (2002) The Cretaceous superchron geodynamo: Observations near the tangent cylinder. *Proc Natl Acad Sci USA* 99:14020–14025.
105. Zhang N, Zhong S (2011) Heat fluxes at the Earth's surface and core–mantle boundary since Pangea formation and their implications for the geomagnetic superchrons. *Earth Planet Sci Lett* 306:205–216.

Supplementary Information for

Neoproterozoic glacial origin of the Great Unconformity

C. Brenhin Keller, Jon M. Husson, Ross N. Mitchell, William F. Bottke, Thomas M. Gernon, Patrick Boehnke, Elizabeth A. Bell, Nicholas L. Swanson-Hysell, and Shanan E. Peters

To whom correspondence should be addressed: C. Brenhin Keller
E-mail: cbkeller@dartmouth.edu

This PDF file includes:

Figs. S1 to S16
References for SI reference citations

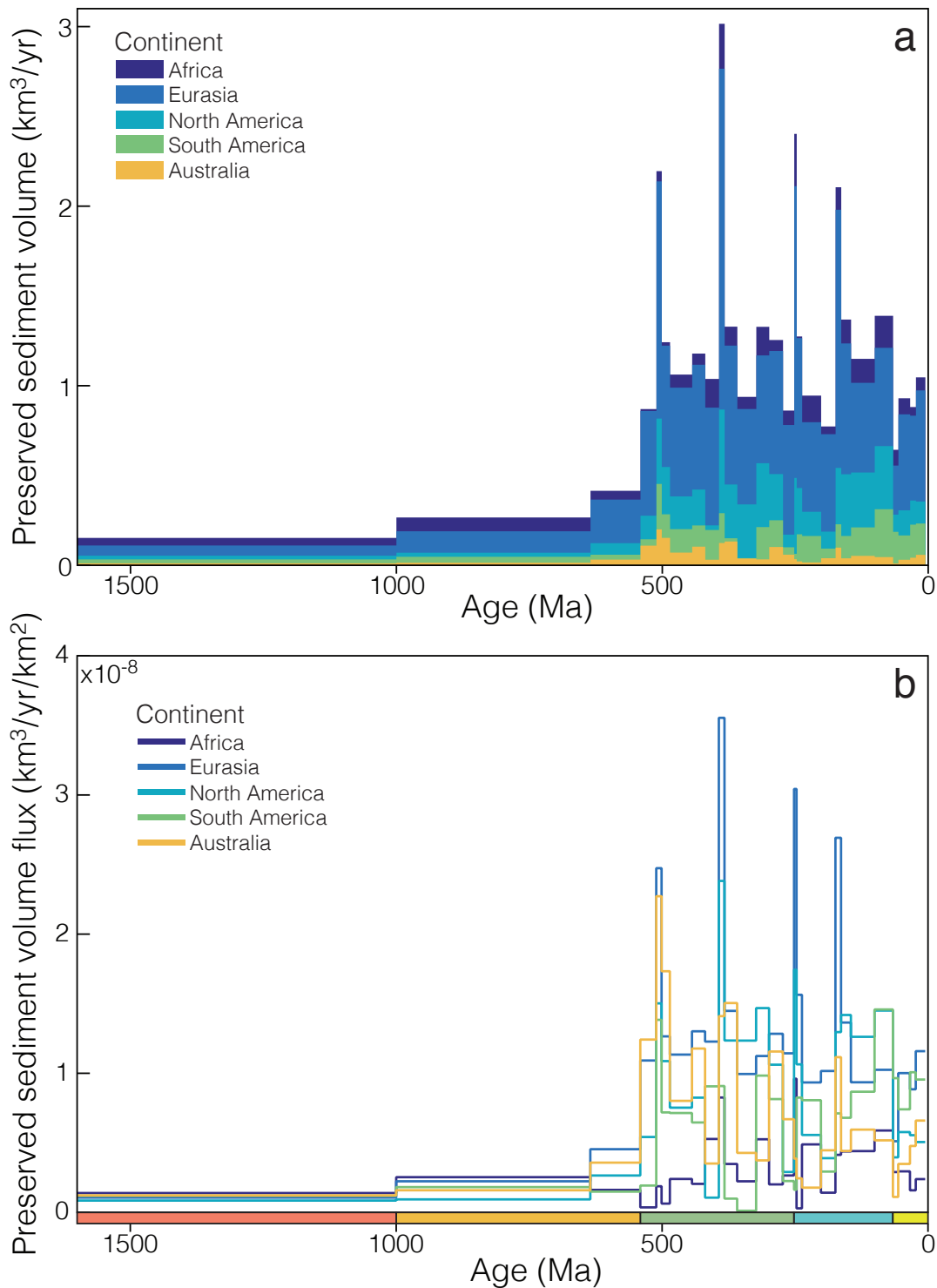


Fig. S1. The volumetric estimates of sedimentation on the continents compiled by Ronov and coauthors (1–15), as tabulated in Dataset S2. **(a)** Preserved sediment volumes for each continent, plotted cumulatively, in km³ per year. **(b)** Volumetric flux, in km³ per year per km² of continental surface area. All continents except Africa display a clear increase in preserved sediment volume and area-normalized sediment flux at the end of the Proterozoic.

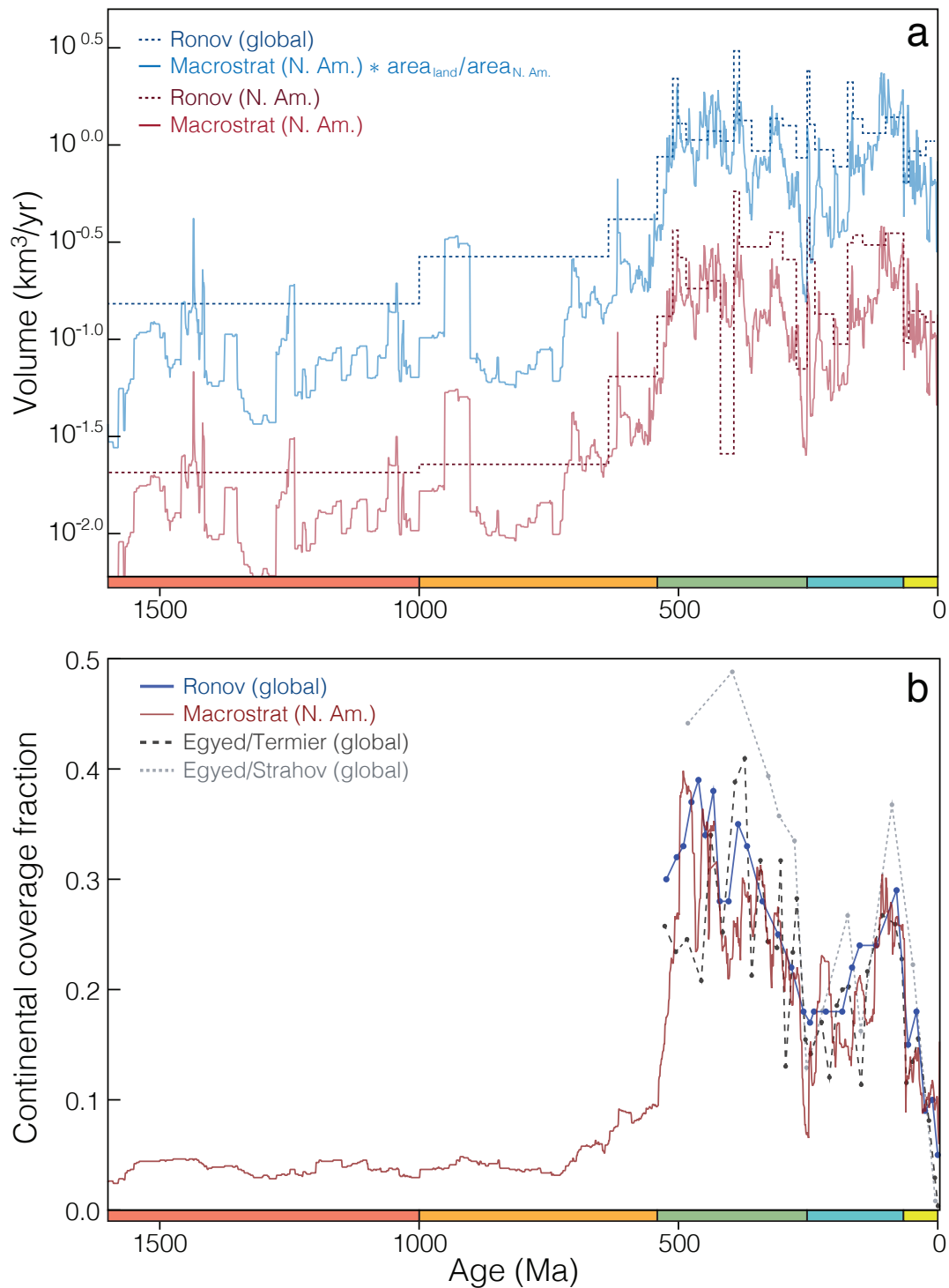


Fig. S2. Comparison of Macrostrat with global records. **(a)** Comparison of Ronov and Macrostrat sedimentary rock volume estimates. Blue: Ronov's (1) global record compared to a global scaling of the North American macrostrat record; that is, the Macrostrat sediment volume estimate for North America multiplied by the area of all continents divided by the area of North America (a factor of 6.1). Red: Ronov and coauthors' (1–15) estimate for preserved sediment volume on North America alone compared to the Macrostrat sediment volume estimate for North America. **(b)** The fraction of continental area covered by marine sediment, as estimated by Macrostrat and three global records: one compiled by Ronov (16), and two compiled by Egyed (17) on the basis of independent paleogeographic atlases, one due to Strahov (18) and the other to Termier & Termier (19).

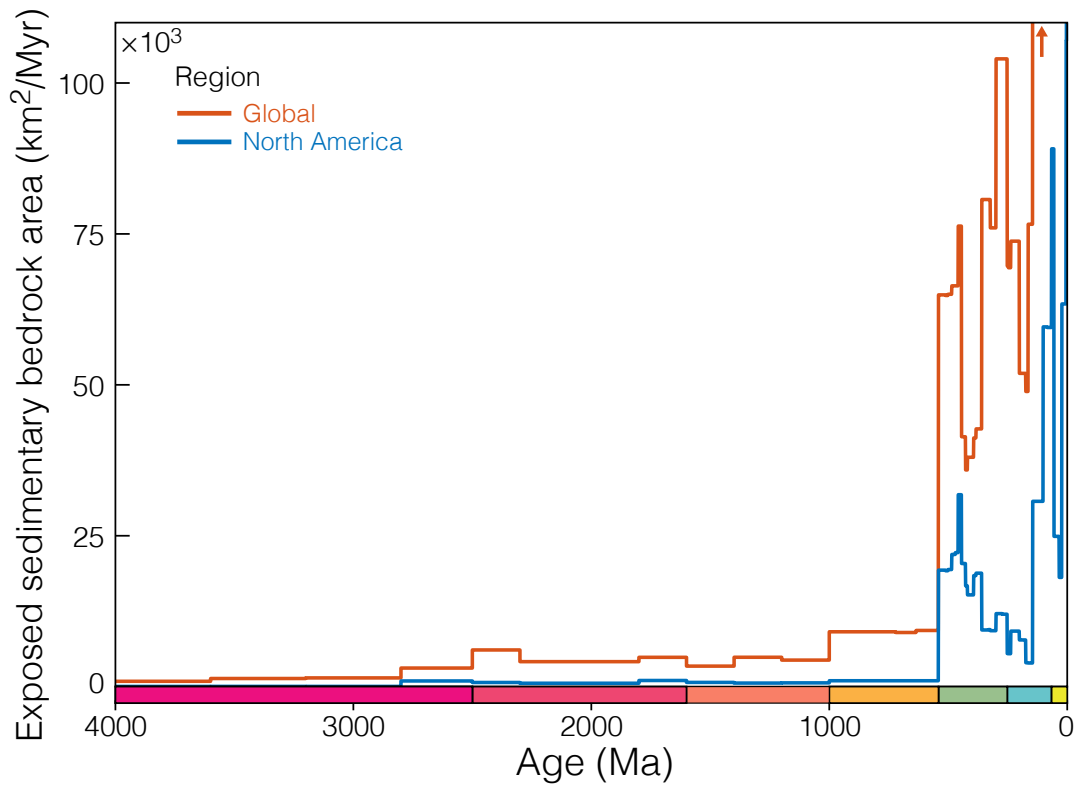


Fig. S3. Exposed surface area of sedimentary and metasedimentary rock as a function of depositional age, derived from the Geological Survey of Canada Generalized Geological Map of the World (20). In comparison to the sedimentary volume record of e.g. Fig. S1, this exposure-area record is significantly biased towards young Tertiary strata because it considers only the exposed uppermost strata of Earth's sedimentary shell. Nonetheless, a major increase in exposed area per unit depositional time is apparent at Proterozoic-Phanerozoic boundary.

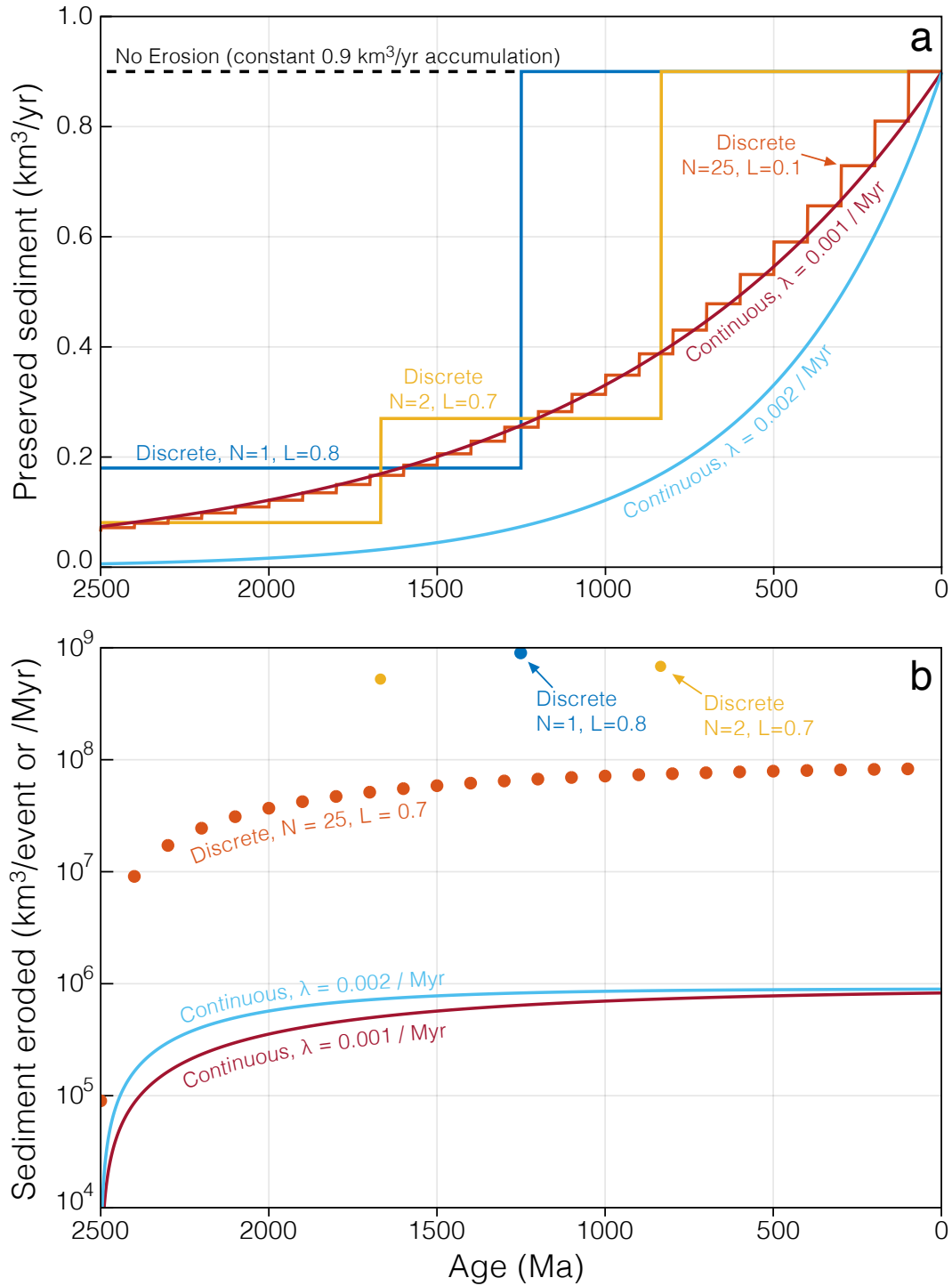


Fig. S4. Effects of continuous and discontinuous erosion in a model with constant $0.9 \text{ km}^3 \text{ y}^{-1}$ sediment input prior to erosion. Following Gregor (21), erosion is assumed to consume preexisting crust in proportion to its abundance. **(a):** Preserved sediment volume per unit time for several imposed continuous and discontinuous erosion scenarios. **(b):** Mass of sediment eroded per event or per unit time, for the same scenarios as in **(a)**. In the discontinuous erosion scenarios, erosion occurs during one or more discrete erosional events, producing step functions in preserved sediment volume. The strength of a given discrete erosional event is specified in terms of a loss factor: $L = 0.8$ specifies an erosional event in which 80% of all accumulated sediment present at the time of the event is eroded. The erosion rate in continuous erosion models, meanwhile, is determined by the decay constant λ , with units of $1/\text{Myr}$. Discontinuous models with N equally-spaced events of identical L converge towards the exponential form of continuous erosion as N becomes large. Note, for instance, the correspondence in preserved volume between the discrete model where 10% of the crust is lost every 100 Myr, and the continuous model with a $\lambda = 0.001/\text{Myr}$ (i.e., 10%/100 Myr).

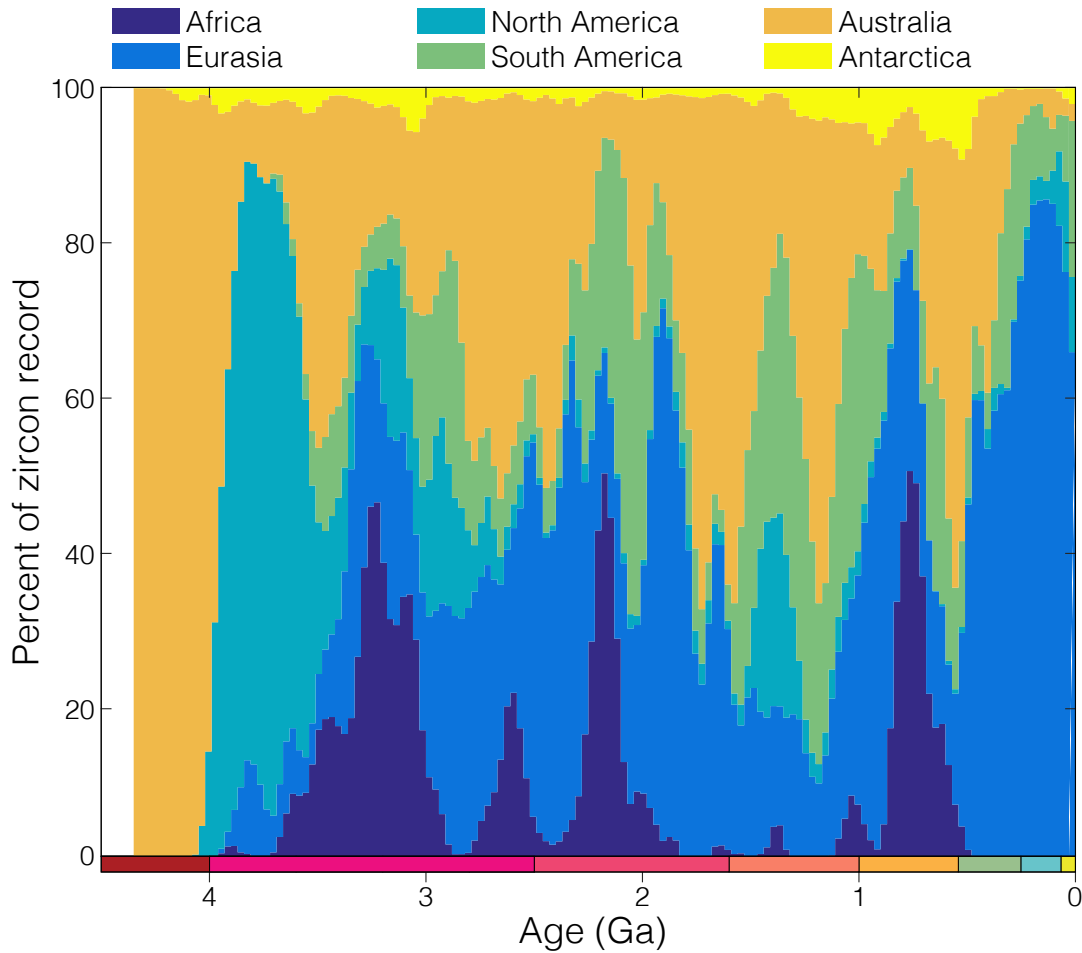


Fig. S5. Geographic distribution (by continent) of zircon Hf and O isotope analyses as a function of zircon U-Pb crystallization age in 200 Myr bins from 0-4.4 Ga. While relative abundances vary episodically in response to tectonic processes, no single continent dominates after 4 Ga.

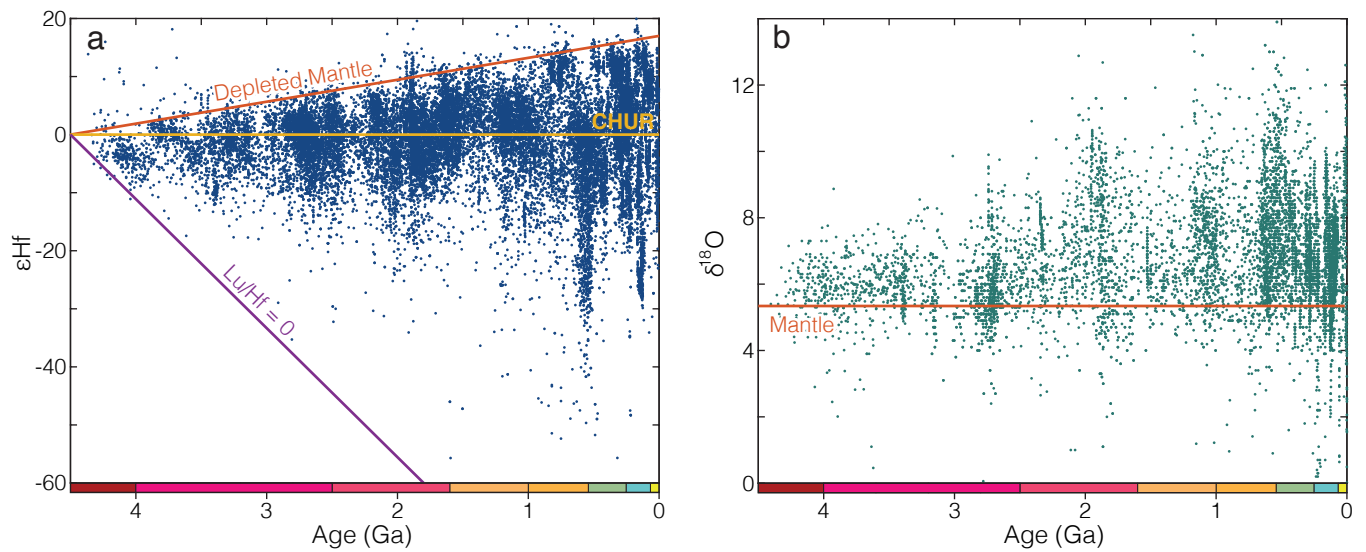


Fig. S6. All data points in the raw compiled zircon Hf and O (**b**) isotope datasets. The Hf isotope record (**a**) is constrained by the composition of the depleted mantle as a rough upper bound and the composition of a hypothetical preserved 4.5 Ga lithology with Lu/Hf = 0 as a strict lower bound. The zircon O isotope record is drawn to supra-mantle $\delta^{18}\text{O}$ by assimilation of siliciclastic sediment or silicate rock that has undergone low-temperature aqueous alteration.

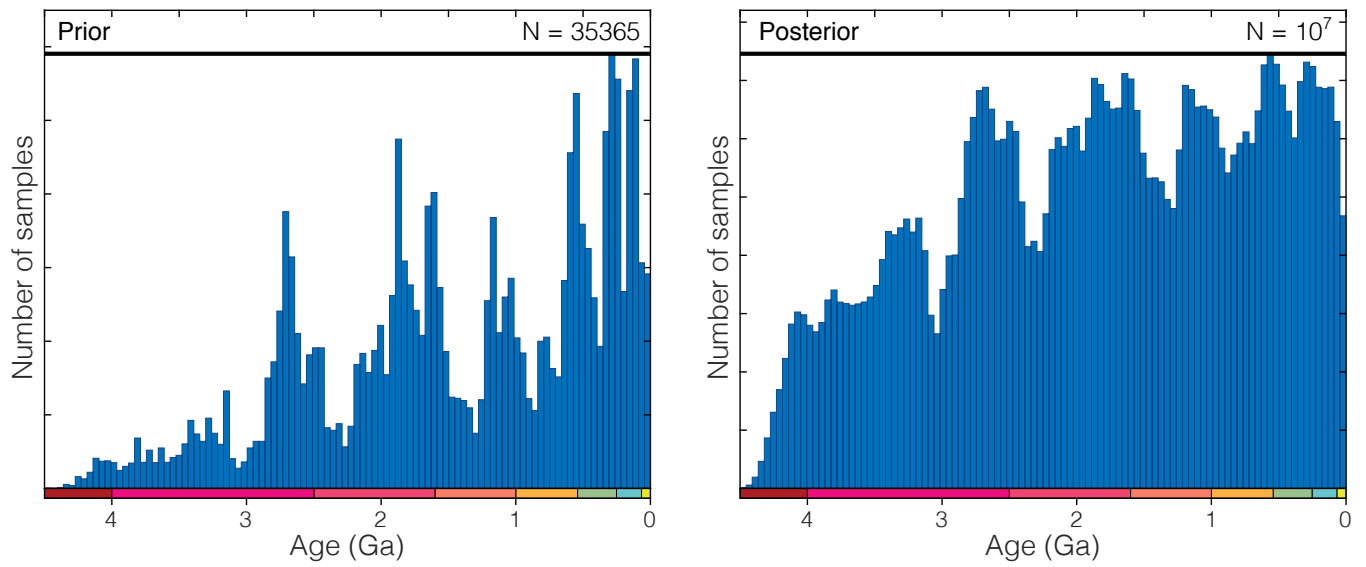


Fig. S7. Zircon age distributions of the raw dataset (prior) and the bootstrap-resampled dataset (posterior). Sample weighting results in a visibly more even posterior distribution.

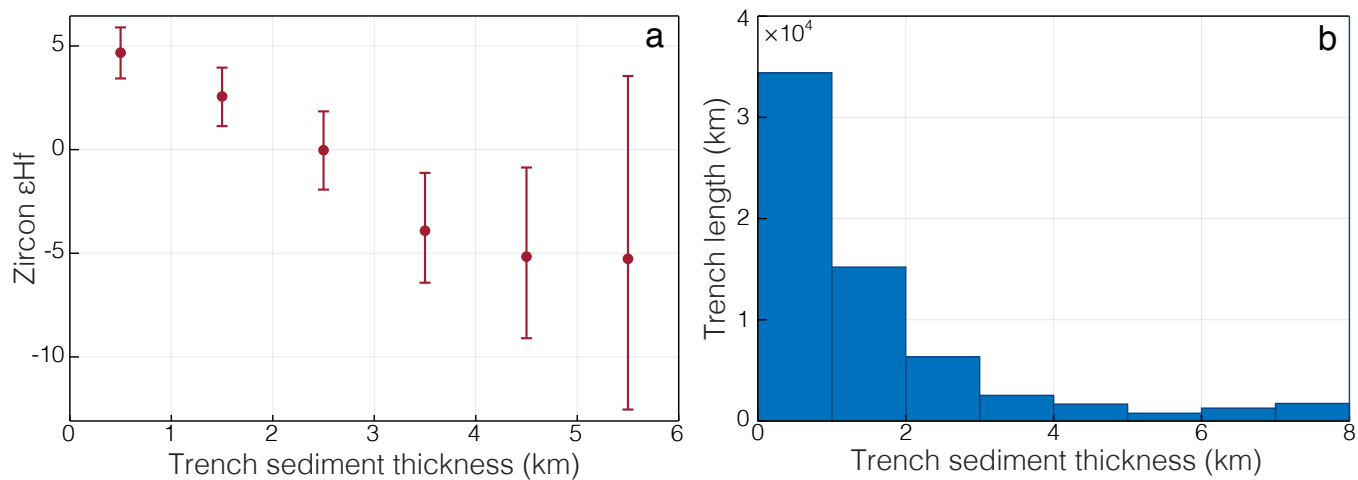


Fig. S8. The importance of sediment subduction to arc magma Hf isotope systematics is demonstrated by the clear variation in average zircon ϵ_{Hf} as a function of present day trench sediment thickness for arc zircons younger than 100 Ma within 5 arc degrees of a trench of known sediment thickness following the sediment thickness maps of Heuret et al. (22) and the geospatially-resolved zircon Hf database of Bataille et al. (23). These data are resampled to accurately represent uncertainty in trench sediment thickness and binned in 1 km intervals. Extreme zircon Hf isotope compositions below $-25 \epsilon_{\text{Hf}}$ are excluded, though this does not visibly influence the resulting trend.

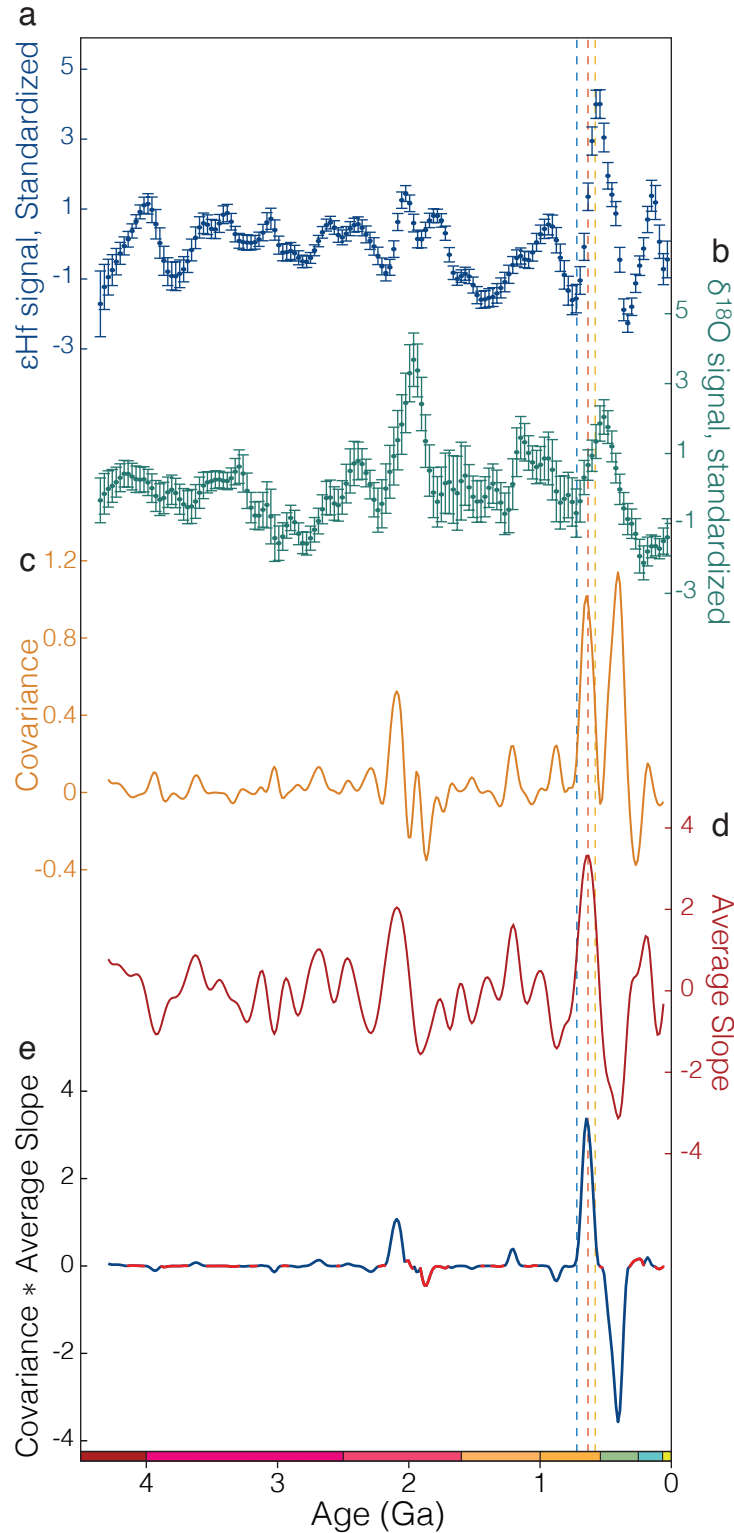


Fig. S9. Determination of sediment subduction signatures. **(a)** The zircon ϵHf record detrended, inverted, and standardized to unit variance; larger values indicate more recycling of old crust into new magmatic zircon. **(b)** The zircon $\delta^{18}\text{O}$ record, detrended and standardized to unit variance; larger values indicate more recycling of surficially altered crust. **(c)** The covariance between **a** and **b**. **(d)** The average slope of **a** and **b**. **(e)** The product of **c** and **d**, color coded blue at times of positive covariance and red at times of negative covariance. As explained in the Methods, sediment subduction events should appear as pairwise excursions with a positive peak for initiation and negative one for recovery.

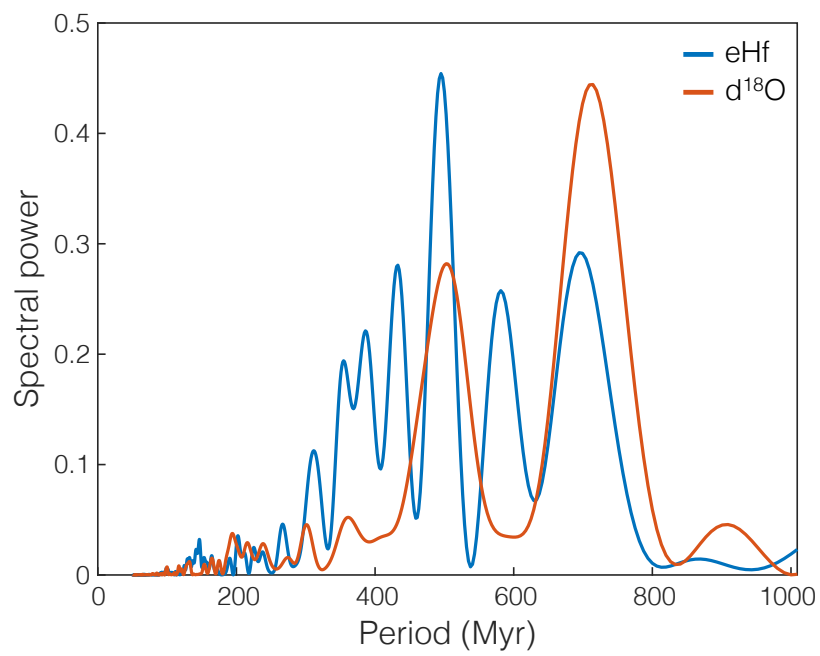


Fig. S10. Periodogram of the zircon Hf and O isotope records, highlighting substantial spectral power at 500-700 Myr periods consistent with tectonic cyclicity.

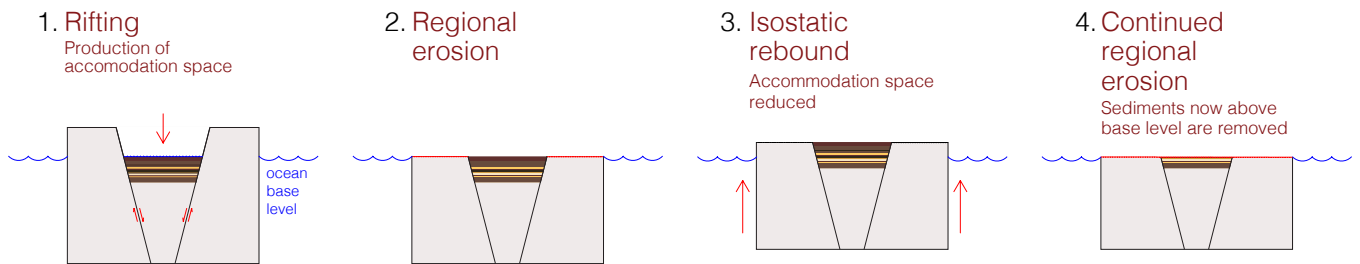


Fig. S11. Illustration of the competition between local tectonic subsidence and regional isostatic uplift under the influence of regional erosion. **1:** Accommodation space is produced by local rifting. **2:** Erosion removes regional uplands (horsts, in this case). **3:** Regional isostatic rebound. **4:** The tectonically-produced basin is now subject to destruction by continued regional erosion. The basin will survive if the rate of tectonic subsidence meets or exceeds the rate of regional erosion. If the rate of tectonic subsidence exactly matches the regional isostatic uplift from upland erosion, the basin will survive intact but with no new accumulation of sediments during the interval of regional erosion. In reality, isostatic rebound will occur continuously in concert with erosion; the two are separated here only to illustrate the underlying principle.

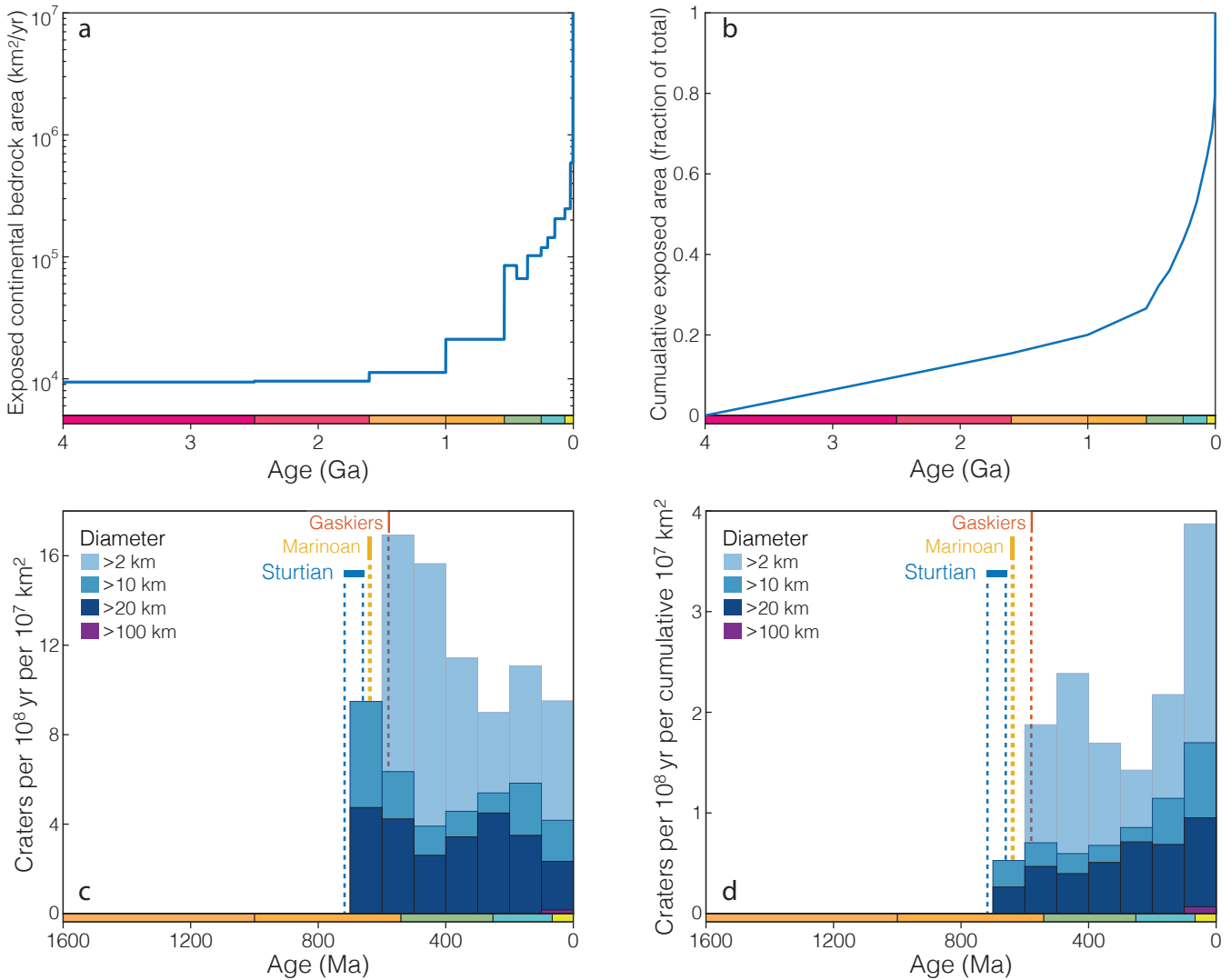


Fig. S12. Comparison of direct versus cumulative area normalizations of impact cratering rate. **(a)** Age distribution of continental bedrock exposed at the present day, derived from the Geological Survey of Canada Generalized Geological Map of the World (20). **(b)** Normalized cumulative age distribution of continental bedrock, obtained by integrating **a** from 4 Ga to time t . The cumulative total (1.0) is equal to the area of the continents, or 1.489×10^8 km². **(c)** Impact cratering rate normalized by raw bedrock exposure from **a**; for sedimentary and volcanic bedrock, we know that this bedrock must have been exposed and susceptible for impact cratering at the time of deposition. **(d)** Impact cratering rate normalized by cumulative bedrock exposure from **b**.

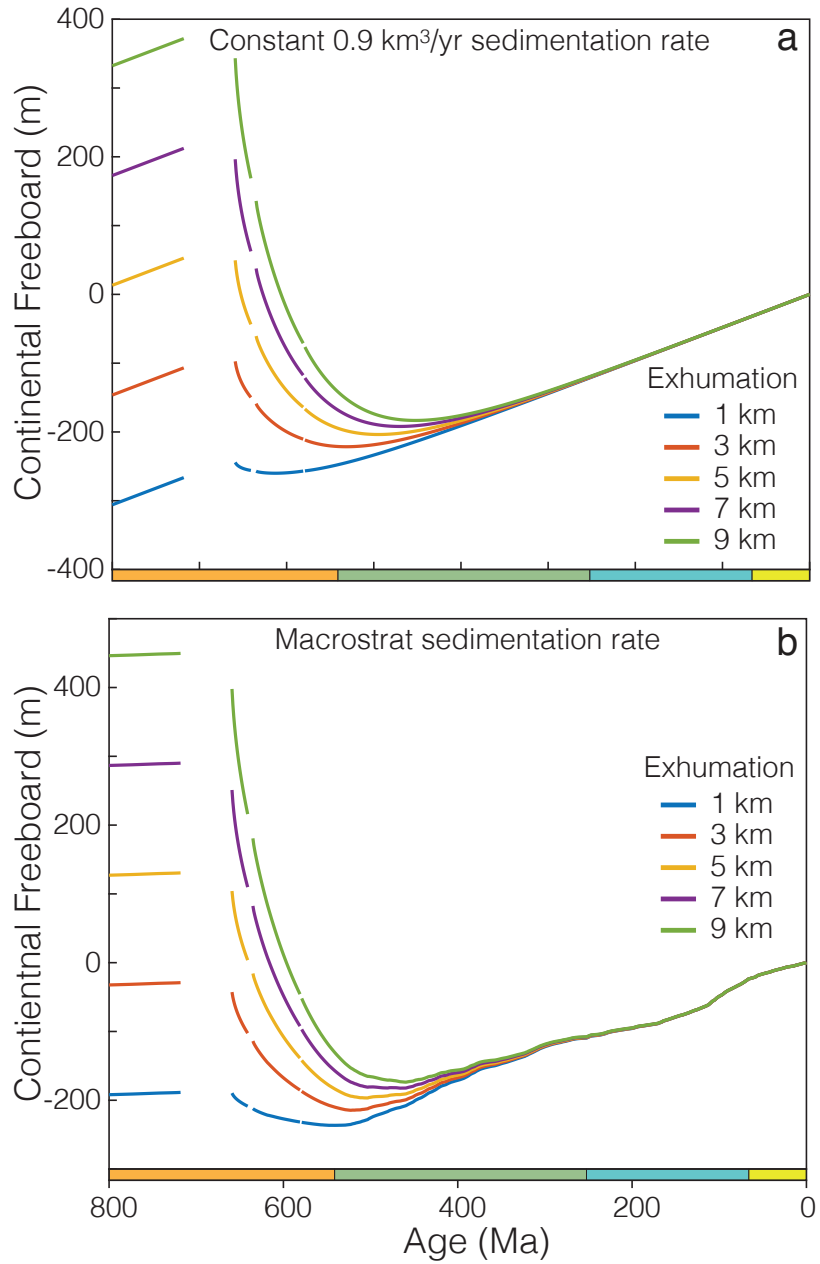


Fig. S13. The effect of variable magnitudes of Neoproterozoic erosion in an isostatic global sea level and continental coverage model. Here, the magnitude of glacial exhumation is varied between 1 and 9 km. Present-day sea level prior to the Neoproterozoic is reproduced with ~ 4.5 km glacial erosion in the constant sedimentation model (a), and ~ 3.5 km in the variable sedimentation model (b).

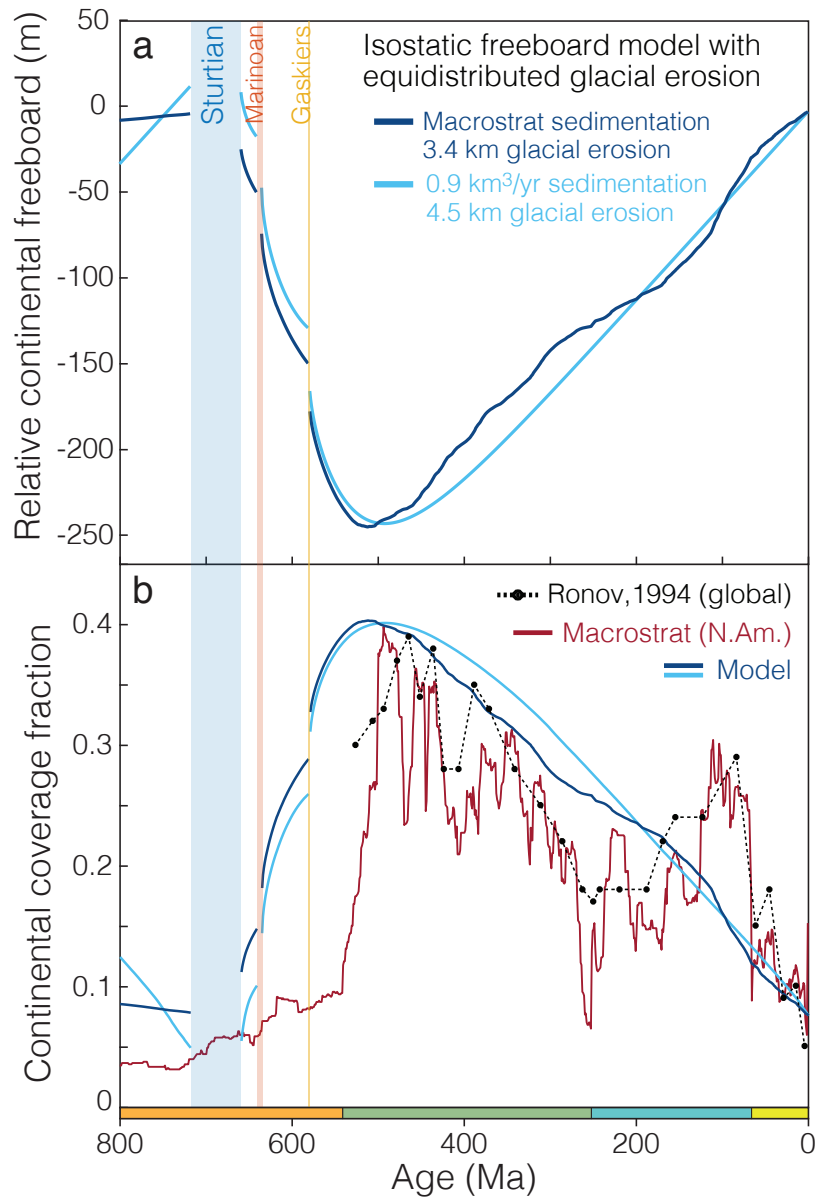


Fig. S14. Isostatic global sea level and continental coverage model, as in Fig. 4, but with glacial erosion equally distributed between the three glacial episodes. **(a)** Temporal evolution in average continental freeboard driven by erosion, subsequent thermal subsidence, and sediment accumulation. **(b)** Corresponding continental coverage fraction.

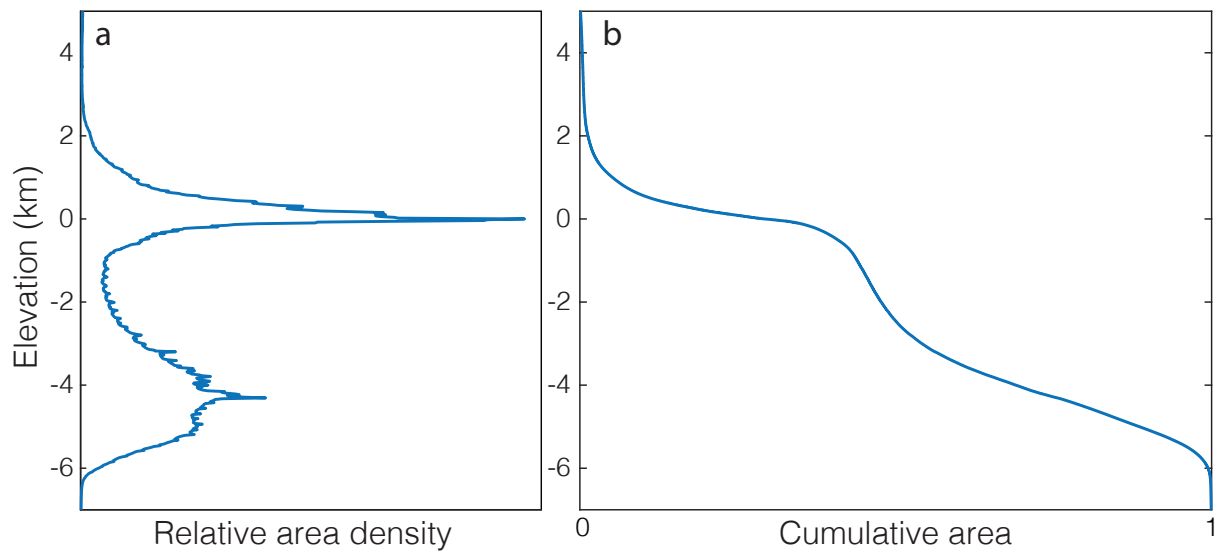
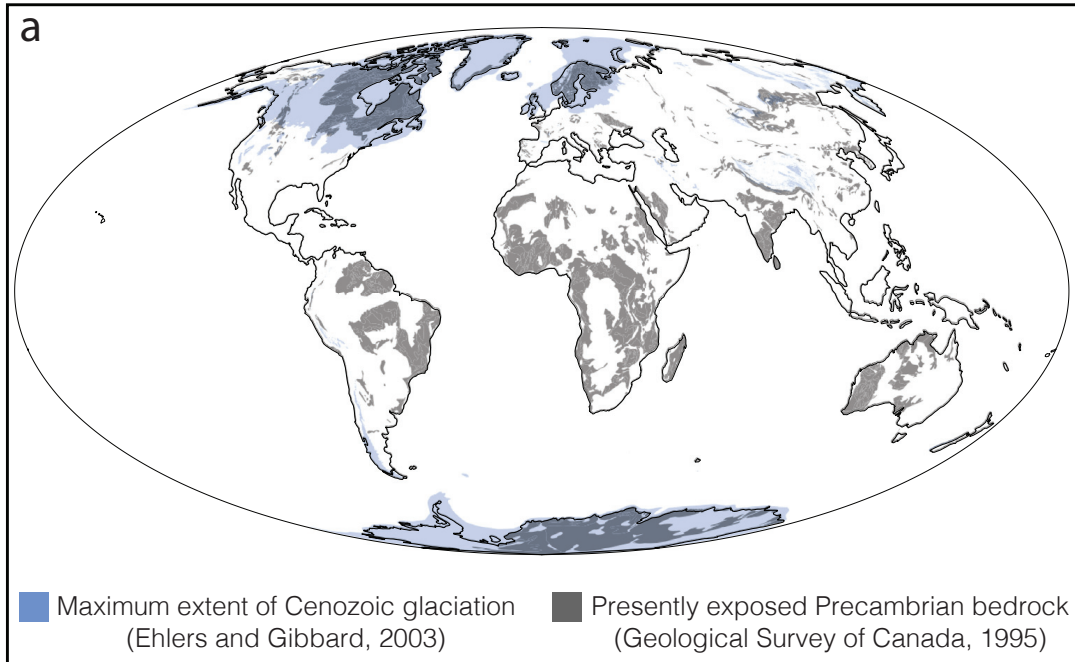


Fig. S15. Earth's present-day hypsometric curve, calculated from the ETOPO1 1 Arc-Minute Global Relief Model (24). The contrast between more dense oceanic crust and more buoyant continental crust is reflected in the clear bimodality in the distribution of elevations. **(a)** An estimate of Earth's elevation distribution based on the elevation of ETOPO1 grid cells. **(b)** Earth's cumulative elevation distribution, obtained by integrating **a** from high to low elevation. A cumulative area of 1.0 corresponds to the total surface area of the Earth.

Precambrian bedrock exposure



Extent of late Paleozoic glaciation

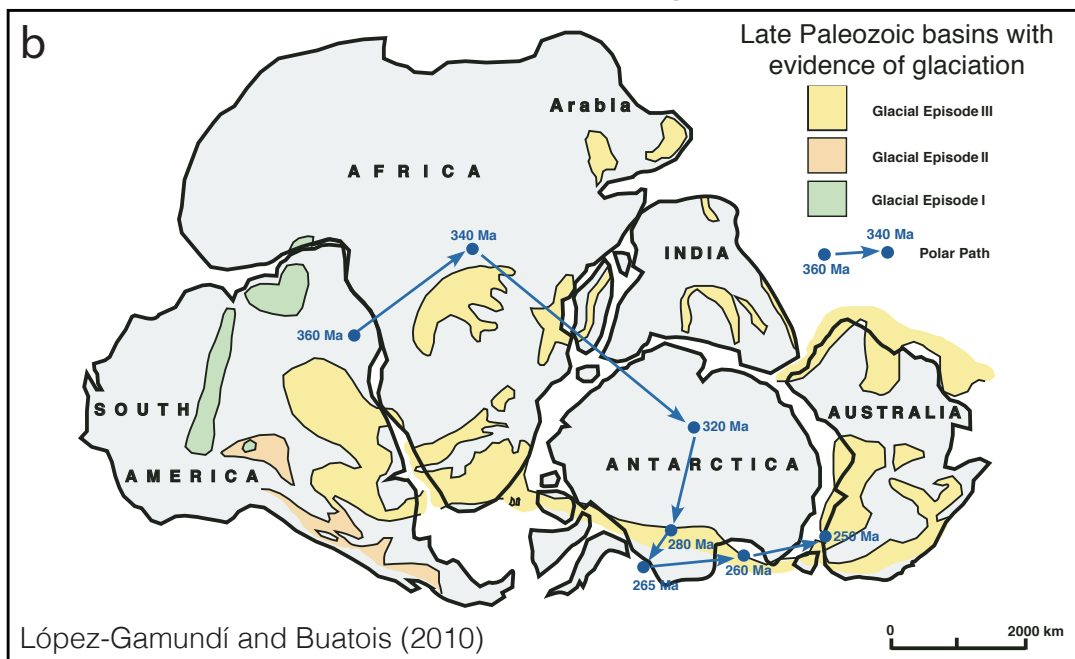


Fig. S16. Global correspondence between Precambrian basement exposures and Phanerozoic glaciation, as first noted by White (1972) (25). **(a)** Major exposures of Precambrian basement from the Geological Survey of Canada Generalized geological map of the world (20) overlain with the maximum extent of Cenozoic glaciation as compiled by Ehlers and Gibbard (26). **(b)** The extent of the Late Paleozoic Ice Age, modified with permission from ref. (27). Virtually all non-orogenic Precambrian basement exposures not covered by Pleistocene glaciation are of Gondwanan affinity, and were likely glaciated during the Late Paleozoic Ice Age. The correspondence between Gondwanan LPIA glaciation and basement exposure is less complete than that between Laurentide glaciation and the Canadian shield (Fig. 5), given that significant proportions of the glaciated area have been covered by Mesozoic and Cenozoic sediment in the intervening ~250 Myr.

References

1. Ronov AB, Khain VE, Balukhovskiy AN, Soslavinskiy KB (1980) Quantitative analysis of Phanerozoic sedimentation. *Sedimentary Geology* 25(4):311–325.
2. Ronov AB, Khain VY, Soslavinskiy KB (1982) Lower and middle Riphean lithologic complexes of the world. *International Geology Review* 24(5):509–525.
3. Khain VY, Ronov AB, Soslavinskiy KB (1982) Upper Riphean lithologic complexes of the world. *International Geology Review* 24(9):993–1008.
4. Ronov AB, Khain VE, Soslavinskiy KB (1981) Vendian lithological complexes of the world. *Soviet Geology* (5):37–59.
5. Ronov AB, Soslavinskiy KB, Khain VY (1977) Cambrian lithologic associations of the world. *International Geology Review* 19(4):373–394.
6. Ronov AB, Khain VY, Soslavinskiy KB (1976) Ordovician lithologic associations of the world. *International Geology Review* 18(12):1395–1412.
7. Khain VY, Ronov AB, Soslavinskiy KB (1978) Silurian lithologic associations of the world. *International Geology Review* 20(3):249–268.
8. Ronov AB, Khain VE (1954) Devonian lithological formations of the world. *Soviet Geology* 41:46–76.
9. Ronov AB, Khain VE (1955) Carboniferous lithological formations of the world. *Soviet Geology* 48:92–117.
10. Ronov AB, Khain VE (1956) Permian lithological formations of the world. *Soviet Geology* 54:20–36.
11. Ronov AB, Khain VE (1961) Triassic lithological formations of the world. *Soviet Geology* (1):27–48.
12. Ronov AB, Khain VE (1962) Jurassic lithological formations of the world. *Soviet Geology* (1):9–34.
13. Khain VY, Ronov AB, Balukhovskiy AN (1976) Cretaceous lithologic associations of the world. *International Geology Review* 18(11):1269–1295.
14. Ronov AB, Khain VY, Balukhovskiy AN (1979) Paleogene lithologic associations of the continents. *International Geology Review* 21(4):415–446.
15. Khain VY, Ronov AB, Balukhovskiy AN (1981) Neogene lithologic associations of the continents. *International Geology Review* 23(4):426–454.
16. Ronov AB (1994) Phanerozoic Transgressions and Regressions on the Continents: a Quantitative Approach Based on Areas Flooded by the Sea and Areas of Marine and Continental Deposition. *American Journal of Science* 294(7):777–801.
17. Egved L (1956) Determination of Changes in the Dimensions of the Earth from Palæogeographical Data. *Nature* 178(4532):534–534.
18. Strahov NM (1948) *Outlines of Historical Geology*, in 2 volumes. (State Publishing Co. Geol. Lit., Moscow).
19. Termier H, Termier G (1953) *Histoire Géologique de la Biosphère*, La vie et les sédiments dans les géographies successives. (Masson et Cie, Éditeurs, Paris).
20. Geological Survey of Canada (1995) Generalized geological map of the world and linked databases, Technical Report 2915d.
21. Gregor B (1970) Denudation of the Continents. *Nature* 228(5268):273–275.
22. Heuret A, Conrad CP, Funicello F (2012) Relation between subduction megathrust earthquakes, trench sediment thickness and upper plate strain. *Geophysical Research Letters* 39.
23. Bataille CP, Willis A, Yang X, Liu XM (2017) Continental igneous rock composition: A major control of past global chemical weathering. *Science Advances* 3(3):e1602183.
24. Amante C, Eakins BW (2009) *ETOPO1 1 arc-minute global relief model: procedures, data sources and analysis* (National Geophysical Data Center, NOAA).
25. White WA (1972) Deep Erosion by Continental Ice Sheets. 83:1037–1056.
26. Ehlers J, Gibbard PL (2003) Extent and chronology of glaciations. *Quaternary Science Reviews* 22(15-17):1561–1568.
27. López-Gamundí OR, Buatois LA (2010) Introduction: Late Paleozoic glacial events and postglacial transgressions in Gondwana in *Geological Society of America Special Paper 468*. (Geological Society of America), pp. v–viii.